AGU PUBLICATIONS

Geochemistry, Geophysics, Geosystems

RESEARCH ARTICLE
10.1002/2017GC007208

Key Points:
- We document magnetic iron sulfide formation associated with methanogenesis across the PETM
- Our results provide rare direct evidence for methane mobilization during the PETM
- Our approach can be used to identify authigenic mineral signatures of methane mobility in ancient sediments

Supporting Information:
- Table S1–S3

Correspondence to:
M. Rudmin,
rudminma@tpu.ru

Citation:
Rudmin, M., Roberts, A. P., Horng, C.-S., Mazurov, A., Savinova, O., Ruban, A., . . . Veklich, M. (2018). Ferrimagnetic iron sulfide formation and methane venting across the Paleocene-Eocene thermal maximum in shallow marine sediments, ancient West Siberian Sea. *Geochemistry, Geophysics, Geosystems*, *19*, 21–42. https://doi.org/10.1002/2017GC007208

Received 31 AUG 2017
Accepted 25 NOV 2017
Accepted article online 4 DEC 2017
Published online 7 JAN 2018

Ferrimagnetic Iron Sulfide Formation and Methane Venting Across the Paleocene-Eocene Thermal Maximum in Shallow Marine Sediments, Ancient West Siberian Sea

Maxim Rudmin[1], Andrew P. Roberts[2], Chorng-Shern Horng[3], Aleksey Mazurov[1], Olesya Savinova[1], Aleksey Ruban[1], Roman Kashapov[1], and Maxim Veklich[4]

[1]Department of Geology and Mineral Exploration, Institute of Natural Resources, Tomsk Polytechnic University, Tomsk, Russia, [2]Research School of Earth Sciences, The Australian National University, Canberra, Australian Capital Territory, Australia, [3]Institute of Earth Sciences, Academia Sinica, Nangang, Taipei, Taiwan, [4]Tomsk Oil and Gas Research and Design Institute, Tomsk, Russia

Abstract Authigenesis of ferrimagnetic iron sulfide minerals (greigite and monoclinic pyrrhotite) occurred across the Paleocene-Eocene Thermal Maximum (PETM) within the Bakchar oolitic ironstone in southeastern Western Siberia. Co-occurrence of these minerals is associated with diagenetic environments that support anaerobic oxidation of methane, which has been validated by methane fluid inclusion analysis in the studied sediments. In modern settings, such ferrimagnetic iron sulfide formation is linked to upward methane diffusion in the presence of minor dissolved sulfide ions. The PETM was the most extreme Cenozoic global warming event and massive methane mobilization has been proposed as a major contributor to the globally observed warming and carbon isotope excursion associated with the PETM. The studied sediments provide rare direct evidence for methane mobilization during the PETM. Magnetic iron sulfide formation associated with methanogenesis in the studied sediments can be explained by enhanced local carbon burial across the PETM. While there is no strong evidence to link local methane venting with more widespread methane mobilization and global warming, the magnetic, petrographic, and geochemical approach used here is applicable to identifying authigenic minerals that provide telltale signatures of methane mobility that can be used to assess methane formation and mobilization through the PETM and other hyperthermal climatic events.

1. Introduction

Ferrimagnetic iron sulfide minerals in marine sediments, including greigite (Fe_3S_4) and monoclinic pyrrhotite (Fe_7S_8), can provide important information about geological, environmental, and diagenetic processes (Berner, 1984; Canfield & Berner, 1987; Horng & Roberts, 2006; Roberts, 2015). Understanding the origin of these minerals also enables assessment of the reliability of sedimentary paleomagnetic signals (Horng et al., 1998; Horng & Huh, 2011; Horng & Roberts, 2006; Kars & Kodama, 2015b; Roberts, 2015; Roberts et al., 2011; Roberts & Weaver, 2005). Sedimentary magnetic iron sulfides can have diagenetic (Kars & Kodama, 2015a; Larrasoaña et al., 2007; Liu et al., 2004; Roberts et al., 2011; Roberts & Turner, 1993; Weaver et al., 2002), biogenic (Chang et al., 2014; Pósfai et al., 2001; Vasiliev et al., 2008), detrital (Horng et al., 2012; Horng & Roberts, 2006), or hydrothermal (Dill et al., 1994; Seewald et al., 1990) origins. Greigite can form in association with early diagenetic processes (Roberts, 2015) such as sulfate reduction (Liu et al., 2004), anaerobic oxidation of methane (Jørgensen et al., 2004; Kasten et al., 1998; Neretin et al., 2004), and formation of methane hydrates (Housen & Musgrave, 1996; Kars & Kodama, 2015a; Larrasoaña et al., 2007). The kinetics of monoclinic pyrrhotite formation preclude its formation during earliest burial; its presence as an authigenic mineral is indicative of formation over longer periods (e.g., Horng & Roberts, 2006), often in relation to anaerobic oxidation of methane and formation of gas hydrates (Horng & Chen, 2006; Kars & Kodama, 2015a; Roberts et al., 2010; Shi et al., 2017; van Dongen et al., 2007; Weaver et al., 2002). The formation of these magnetic iron sulfide minerals (particularly pyrrhotite) has been associated with increasingly methane seepage in marine sediments (Jørgensen et al., 2004; Kars & Kodama, 2015a, 2015b; Larrasoaña et al., 2007; Neretin et al., 2004; van Dongen et al., 2007). This is important because methane emissions are a leading cause of past global climate change (Kvenvolden, 1993) and contribute to present-day climate change (Crichton et al., 2016; Monnin, 2001; Shakhova et al., 2017; Tesi et al., 2016).

The Paleocene-Eocene Thermal Maximum (PETM), across which the studied sediments were deposited, was the most extreme Cenozoic global warming event (Bowen et al., 2004; Kennett & Stott, 1991; Thomas & Shackleton, 1996; Zachos et al., 2003, 2008), and was characterized by a 5–8°C worldwide warming of Earth's surface, which included deep ocean warming (Dunkley Jones et al., 2013; McInerney & Wing, 2011). Marine and terrestrial records document a global 1.5–6‰ mean negative carbon isotope excursion (CIE) (Kennett & Stott, 1991; Koch et al., 1992; Manners et al., 2013; McInerney & Wing, 2011; Stassen et al., 2015; Thomas & Shackleton, 1996; Zhang et al., 2017), and marine sediments provide geochemical and sedimentological evidence for ocean acidification (Griffith et al., 2015; Penman et al., 2014; Zeebe & Zachos, 2007). This indicates that during the PETM, thousands of gigatons of carbon were released into the ocean and atmosphere over several thousand years (Higgins & Schrag, 2006; McInerney & Wing, 2011; Meissner et al., 2014; Zeebe et al., 2016). The aftermath of the paleoenvironmental changes that occurred during the PETM is recorded in sedimentary rocks, and includes increased marine productivity (Bains et al., 2000; Schmitz et al., 1997; Stassen et al., 2015), significant ocean chemistry and circulation changes (Baczynski et al., 2017; Cope & Winguth, 2011; Lunt et al., 2010; Nunes & Norris, 2006), accelerated chemical weathering of terrestrial silicate rocks (Dickson et al., 2015; Fontorbe et al., 2016; Penman, 2016), expansion of anoxic water masses (Dickson et al., 2014), and deepening of the oceanic carbonate compensation depth (Pälike et al., 2014; Panchuk et al., 2008; Penman et al., 2015). As a result of the PETM, about 50% of benthic foraminiferal species became extinct (Alegret et al., 2009; Gibbs et al., 2012; Shcherbinina et al., 2016; Stassen et al., 2015) and terrestrial flora increased their diversity, leaf size, and shape (Jaramillo et al., 2006; Wing et al., 2005).

Massive methane hydrate release has been attributed to be a major cause of dramatic climate change across the Paleocene-Eocene (P-E) boundary (Bowen et al., 2004; Carozza et al., 2011; Dickens et al., 1995; Nunes & Norris, 2006; Thomas et al., 2002; Yamamoto et al., 2009; Zachos et al., 2003). However, direct evidence of methane emissions during the PETM remains limited. In this study, we document the association of ferrimagnetic iron sulfides with methane seepage during the PETM, which provides an opportunity to assess the wider environmental implications of methanic conditions in oolitic ironstones across the P-E boundary from the ancient epicontinental West Siberian Sea.

2. Geological Setting

The Bakchar deposit is the one of the main deposits of the West Siberian iron ore basin (Belous et al., 1964) and is located on the southeastern Western Siberian Plain (Figures 1a and 1b). Based on biostratigraphy, oolitic ironstones of the Bakchar deposit formed from the Cretaceous (Turonian) to the Eocene (Gnibidenko et al., 2015; Lebedeva et al., 2017; Podobina, 1998, 2003, 2015), and occur within marine sandstones, siltstones, and claystones. The ironstones of Western Siberia are confined to the coastal area of the ancient epicontinental West Siberian Sea (Figure 1a) (Frieling et al., 2014; Iakovleva, 2011) and are distributed along the southeastern Western Siberian plain (Belous et al., 1964). In the Late Paleogene and Eocene, the West Siberian Sea (or Obik Sea; Carney & Dick, 2000) was connected to the northeastern Peritethys via the Turgai Seaway and represented one of the main paleogeographic elements of Central Eurasia (Akhmetiev & Zaporozhets, 2014). The Bakchar oolitic ironstones consist of chamosite-goethite ooliths, ooids, and detrital quartz and feldspars in a matrix of hydromica, chamosite, and siderite (Rudmin & Mazurov, 2016). The studied P-E sequence lies immediately above the iron-bearing deposits of the so-called Bakchar horizon. A Paleocene age of the Bakchar horizon is indicated by foraminiferal assemblages that include *Cyclammina coksuvorovae* (*Uschakova*), *Verneuilinoides paleogenicus* (*Lipman*), *Trochammina pentacamerata* (*Lipman*), and *Trochammina intacta* (*Podobina*), while the Eocene age of overlying claystones is indicated by foraminiferal assemblages that include *Textularia carinatiformis sibirica*, *Anomalinoides ypresiensis ovatus*, *Labrospira granulosa* (*Lipman*), and *Ammomarginulina spectata* (*Podobina*) (Podobina, 1998, 2003, 2015). Vibe et al. (2017) indicated that the West Siberian basin experienced varied and prolonged vertical motion from its inception in the Triassic to today. Rapid tectonic subsidence in the Triassic and Early Jurassic was followed by a slowdown in the Late Jurassic-Cretaceous. Slow Paleocene subsidence continued until the Middle Oligocene when the basin experienced renewed uplift. Tectonic subsidence in Jurassic deposits of the southeastern West Siberian basin reached 2.5–3 km, but early Paleogene deposits were associated with uplift (Vibe et al., 2017). This suggests that early Paleogene sediments in the Bakchar deposit did not undergo deep burial, which is supported by their unlithified nature.

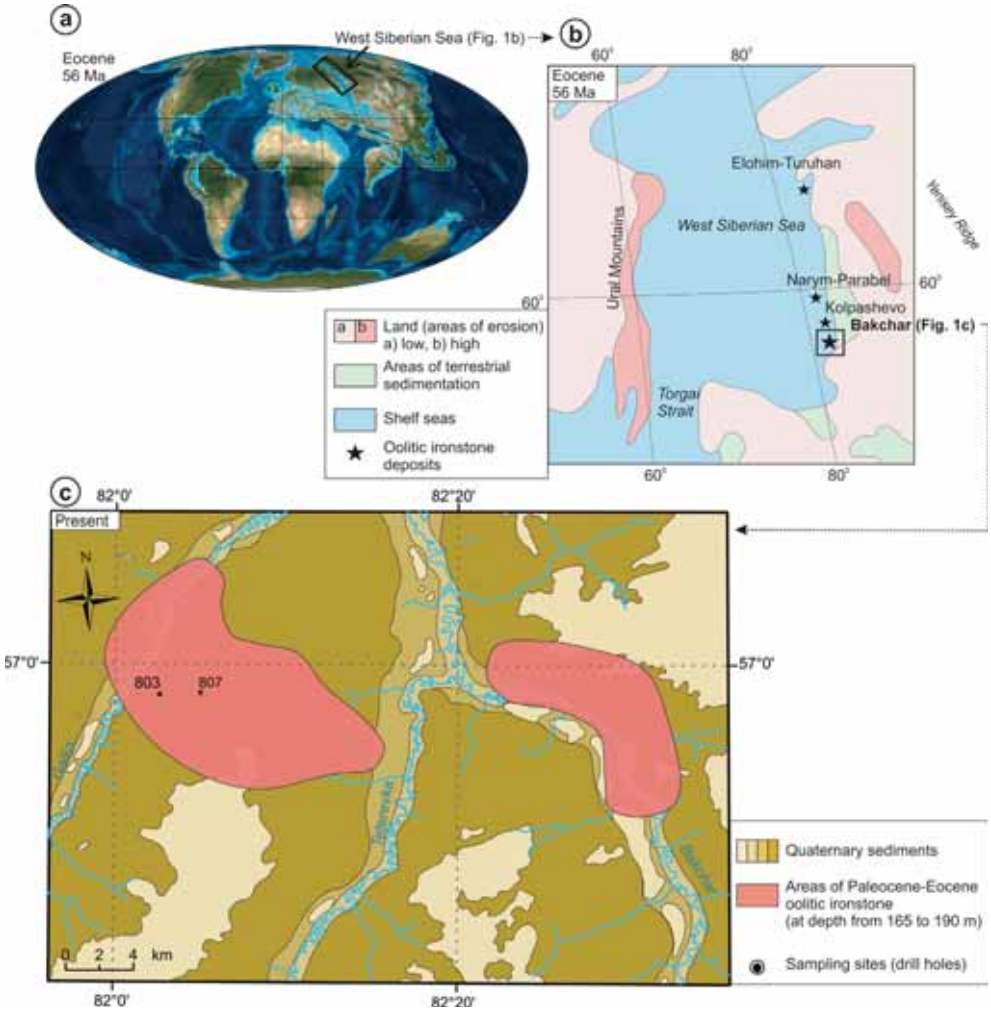

Figure 1. (a) Global Eocene plate reconstruction with location of the West Siberian Sea (modified from http://www2.nau.edu/rcb7/globaltext2.html). (b) Eocene paleogeographic map of the studied region around the West Siberian Sea with locations of oolitic ironstone deposits (modified from Smith et al. (1994)). (c) Simplified geological map of the Bakchar deposit with distribution of Paleocene-Eocene oolitic ironstone (modified from Belous et al. (1964)).

3. Materials and Methods

More than 40 oolitic ironstone samples (with high magnetic susceptibility, MS) were collected from drill cores (Figure 1c) from the 155 to 192 m cored depth interval of P-E sedimentary rocks of the Bakchar deposit and were investigated with mineralogical, petrographic, and geochemical techniques. MS measurements were made directly on the core with a Terraplus KT-10 MS meter (sensitivity of 1×10^{-6} SI). Measurements were made at 10 cm stratigraphic intervals for 645 discrete samples.

Sedimentary iron sulfide minerals, including pyrrhotite, greigite, and pyrite, were identified and investigated using scanning electron microscope (SEM) observations with energy dispersive X-ray spectroscopy (EDS) analyses. SEM-EDS analyses were performed on polished sections, using a TESCAN VEGA 3 SBU SEM equipped with an OXFORD X-Max 50 EDS analyzer with a Si/Li crystal detector. An accelerating voltage of 20 kV with a beam current between 3.5 and 15 nA was used for SEM observations. X-ray fluorescence (XRF) analysis was undertaken to determine the major element chemistry of 30 powdered samples ($<$250 μm) with a HORIBA X-Ray Analytical Microscope XGT 7200, operated at 15–50 kV and 1–100 mA, with a 1.2 mm X-ray beam for 100 s. The detection limit for major elements is better than 0.01 wt %. SEM and XRF

investigations were carried out at the Department of Geology and Minerals Prospecting, Tomsk Polytechnic University.

Trace elements (TEs) were analyzed using inductively coupled plasma-mass spectroscopy (ICP-MS) at the Hydrogeochemistry Research Laboratory, Tomsk Polytechnic University. About 0.5 g of powdered sample was fused using 0.8 g of $LiBO_2/Li_2B_4O_7$ at 1,050°C for 15 min. After fusion, the glass beads were dissolved in a mixture of 5:4:1.5 HF, HNO_3, and $HClO_4$ at 120°C in a platinum crucible for 6 h. The acids were evaporated at 160°C; the rest was dissolved in 10 mL of $5HNO_3$. The resultant solutions were filtered and analyzed for rare earth elements (see El-Habaak et al., 2016). All elemental concentrations were normalized to Al content to remove the effect of variable terrigenous input (Brumsack, 2006; Tribovillard et al., 2006). Al commonly has a detrital origin and is usually immobile during biological and diagenetic processes (Calvert & Pedersen, 1993). Enrichment factors (EFs) were calculated for each sample as follows (Tribovillard et al., 2006): X $EF = (X/Al)_{sample}/(X/Al)_{PAAS}$, where $(X/Al)_{PAAS}$ is the aluminum-normalized concentration of element X, ratioed to that of PAAS (post-Archean Australian shale) from Taylor and McLennan (1985). $EF > 1$ represents detectable authigenic enrichment of the element above average shale concentration, where $EF > 10$ indicates moderate to strong enrichment (Núñez-Useche et al., 2016; Tribovillard et al., 2006, 2012). Biogenic barium (Ba_{bio}) was calculated using the normalized approach of Dymond et al. (1992): $Ba_{bio} = Ba_{total} - (Al \times (Ba/Al)_{detrit})$, where $(Ba/Al)_{detrit}$ represents the Ba/Al ratio (0.0037) of the global average ratio proposed by Reitz et al. (2004).

Pyrolysis was performed on samples using a model 6 turbo ROCK-EVAL analyzer (Vinci Technologies) at the Arctic Seas Carbon Research International Laboratory, Tomsk Polytechnic University, where 100 mg samples were heated to 300°C to release volatile hydrocarbons. Pyrolysis was performed at a rate of 25°C/min to 600°C to release pyrolytic hydrocarbons. The CO_2 released was trapped inside a thermal conductivity detector to quantify thermally produced organic CO_2, which is the total organic carbon (TOC) content. In order to constrain the age model and to identify the PETM CIE, samples were analyzed for bulk organic carbon isotopes ($\delta^{13}C_{org}$). $\delta^{13}C_{org}$ analyses were carried out at the Tomsk Oil and Gas Research and Design Institute. An aliquot of each powdered sample was decarbonated using 10% HCl. The samples were analyzed by continuous flow isotope ratio mass spectrometry using a DELTA V ADVANTAGE mass spectrometer (Thermo Fisher Scientific) coupled to an elemental analyzer Flash 2000 through a universal interface ConFlo IV. Carbon isotope abundance is expressed as $\delta^{13}C_{org}$ (‰) relative to VPDB (Vienna Pee Dee Belemnite). International reference standards (NBS-22, IAEA-CH-7, and USGS 24) were used for $\delta^{13}C_{org}$ calibration.

Fluid inclusions were analyzed using a Lincam MDSG600 Heating-Freezing system mounted on a standard petrographic microscope at the Department of Geology and Minerals Prospecting, Tomsk Polytechnic University. The precision for measured temperatures is approximately ±0.1°C from −196°C to 600°C. Freezing and heating temperatures were measured for the same inclusion where possible. A confocal Thermo Fisher Scientific DXR2 Raman spectrometer was used to detect volatile phases in fluid inclusions. All measurements were carried out with a laser wavelength of 532 nm and 20–25 mW power. The beam was focused on the bubble for each fluid inclusion through a light microscope. Spectra were usually acquired over a 30 s period for 0 to 3,300 cm^{-1} with a three-rate accumulation. This accumulation results in unrealistic quantitative intensities, but reduces the background signal significantly. For qualitative evaluation, resulting Raman shifts were compared with the Raman data base of Frezzotti et al. (2012). Raman analyses were carried out at the Department of Geology and Minerals Prospecting, Tomsk Polytechnic University.

4. Results

4.1. Lithology and Petrography

The Paleocene Bakchar sequence has greenish-gray sandstone at the base that is overlain directly by brownish-gray oolitic ironstones (Figure 2). Sandstone thicknesses vary mostly from 2 to 11.5 m and depend on distance from the ancient coast line. The Paleocene deposits overlie Maastrichtian oolitic ironstones or glauconitic sandstones. The Paleocene ironstones are lenticular bodies with northwest-southeast striking orientations. The thickness of these oolitic ironstones varies from 2.5 to 22 m. The P-E Bakchar horizon consists of two types of ores: loose oolitic ironstone (thickness 0.2–11.4 m) occurs at the base of the horizon and is replaced higher in the section by cemented oolitic ironstone with siderite matrix (thickness 0.2–7.7 m). Eocene parallel-laminated hydromica claystone overlies the Paleocene ironstone discordantly

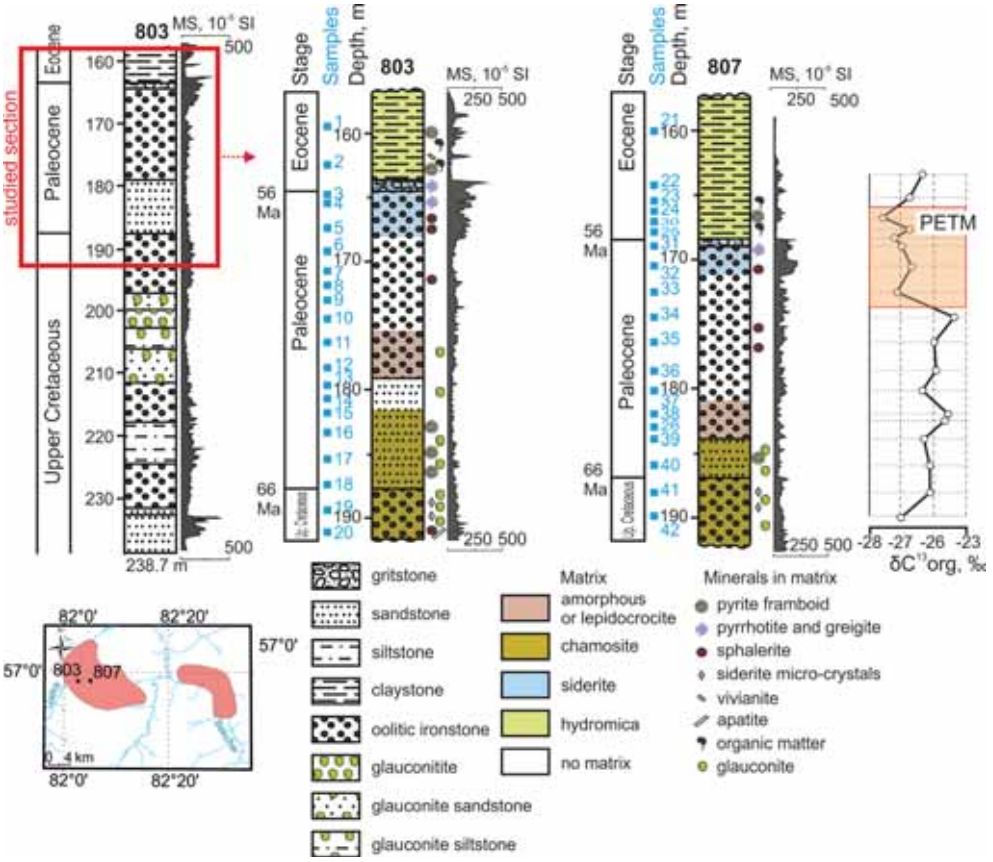

Figure 2. Stratigraphic columns of the Bakchar deposit with magnetic susceptibility (MS) profiles.

and consists of a complex of detrital materials with gritstone (thickness 0.1–1.1 m) at the base. The Eocene claystones have average thicknesses of 12.5 m.

The Maastrichtian oolitic ironstones (Figure 3a) are brownish-gray, medium-grained, and comprise terrigenous material (30–40%), chamosite-goethite ooids (20–25%), glauconite (8–20%), and chamosite matrix. Microcrystals of siderite, rare sphalerite, pyrite framboids, or apatite are observed in the chamosite matrix of these rocks. Maastrichtian glauconitic sandstones are greenish-gray and fine-grained, and consist of detrital quartz (40–54%), glauconite (22–33%), chamosite-goethite ooids (5–20%), and chamosite matrix. The Paleocene sandstone (Figure 3b) is yellowish-gray or greenish-gray, medium-grained, and comprises detrital quartz and feldspars (55–60%), chamosite-goethite ooids (10–45%), glauconite (5–15%), pyrite framboids, and chamosite matrix. The oolitic ironstone with amorphous or lepidocrocite matrix (Figure 3c) consists of quartz (20–30%), chamosite-goethite ooids (40–60%), and glauconite (up to 5%). The loose ironstone (Figure 3e) is dark-brown to black, medium-grained and comprises chamosite-goethite ooliths (70–80%), and detrital quartz (20–30%). The cemented ironstone (Figure 3d) is brown, medium-grained, and consists of chamosite-goethite ooliths (50–60%) and detrital quartz (5–10%) in siderite matrix. The Eocene gritstone has a tobacco color (Figure 3f) and comprises large siliciclastic fragments, ooliths, glauconite, and siderite matrix. The Eocene claystone is greenish-gray, parallel-laminated, and often includes siltstone interlayers or lenses (Figure 3g). The claystone consists of hydromica with organic matter, pyrite framboids in siltstone interlayers or lenses, and rare vivianite.

4.2. Magnetic Susceptibility

Volume MS profiles are presented in Figure 2 and Table A1 for the iron-bearing Bakchar deposit (depth interval of 160–240 m) and for the P-E part of the section (depth interval of 155–188 m). MS varies in the range of 2.9–289.2 $\times$ 10^{-5} SI (27.4–66.6 $\times$ 10^{-5} SI, first and third quartiles). While the MS of Paleocene

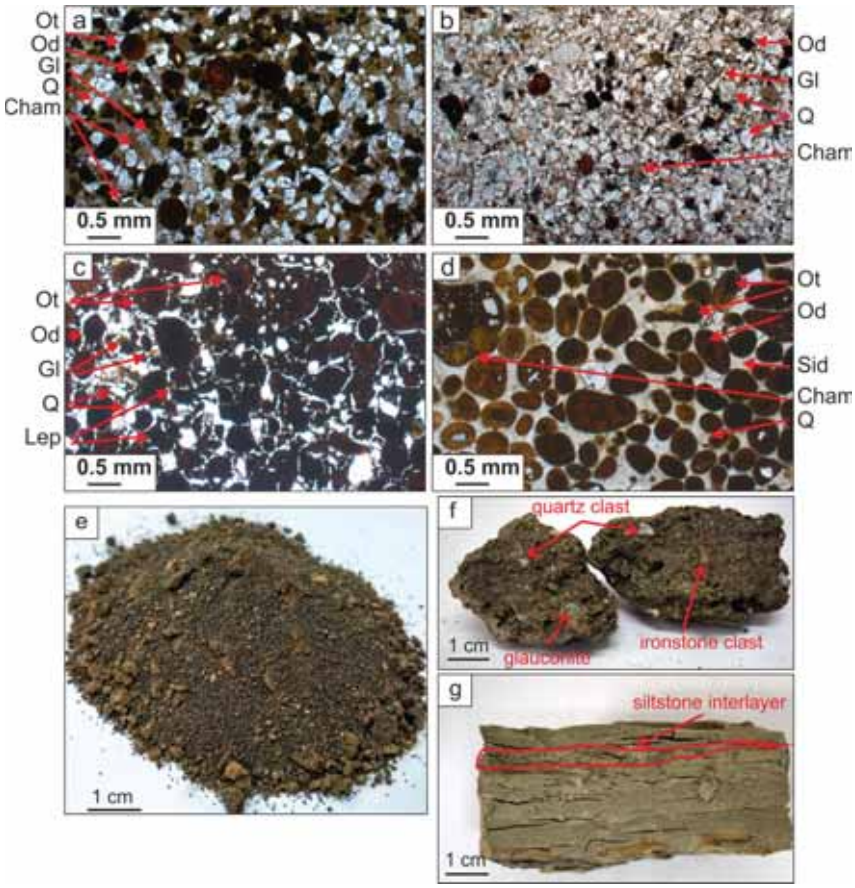

Figure 3. Petrographic thin sections (transmitted light) and photographs of representative samples from different lithologies. (a) Maastrichtian oolitic ironstone with chamosite matrix (sample 19). (b) Paleocene sandstone (sample 16). (c) Paleocene oolitic ironstone with hydrogoethite matrix (sample 11). (d) Paleocene cemented oolitic ironstone with siderite matrix (sample 5). (e) Paleocene loose oolitic ironstone (sample 9). (f) Eocene gritstone with glauconite, ironstone, and quartz clasts (sample 3). (g) Eocene claystone with siltstone interlayer (sample 2). Ot, chamosite-goethite ooliths; Od, chamosite-goethite ooids; Gl, glauconite; Q, quartz; Cham, chamosite matrix; Sid, siderite cement; and Lep, lepidocrocite or amorphous Fe^{3+} matrix.

oolitic ironstones and Eocene claystones is weak with values of 15.6–119.8 $\times$ 10^{-5} SI (42.9–71.8 $\times$ 10^{-5} SI, first and third quartiles) and 2.9–165.4 $\times$ 10^{-5} SI (13.0–39.4 $\times$ 10^{-5} SI, first and third quartiles), respectively, rocks that contain magnetic iron sulfides (siderite-cemented gritstone and oolitic ironstone) have higher MS with values of 64.6–289.2 $\times$ 10^{-5} SI (119.5–172.2 $\times$ 10^{-5} SI, first and third quartiles).

4.3. Sedimentary Microtextures and Mineralogy

Ferrimagnetic iron sulfides (greigite and pyrrhotite) are associated with siderite cement and pyrite within the studied deposits. Pyrite is the dominant iron sulfide, but greigite and pyrrhotite are also often observed in Paleocene oolitic ironstone with siderite cement and in Eocene gritstone. The three dominant textural forms of pyrite in the studied section are framboids (Figures 4a and 4c), polyframboids (Figure 4a), and larger (several μm across) euhedral crystals (Figure 4b). Pyrite framboids consist of sub-μm crystals (Figure 4c). Most framboids occur in polyframboidal aggregates, each of which consists of multiple individual framboids (Figure 4a). The size of pyrite framboids varies from 3 to 46.6 μm. Pyrite framboids prevail in the chamosite or hydromica matrix of oolitic ironstones, sandstones, and siltstones. Pyrite is also observed in the Eocene claystone within siltstone interlayers or lenses (Figure 4a). In the gritstone, pyrite is associated with siderite, greigite, and pyrrhotite (Figure 5). Greigite occurs in irregular and subhedral aggregates (Figure 5a), sometimes in association with pyrite (Figure 5b). The main pyrrhotite occurrence in the studied rocks is in

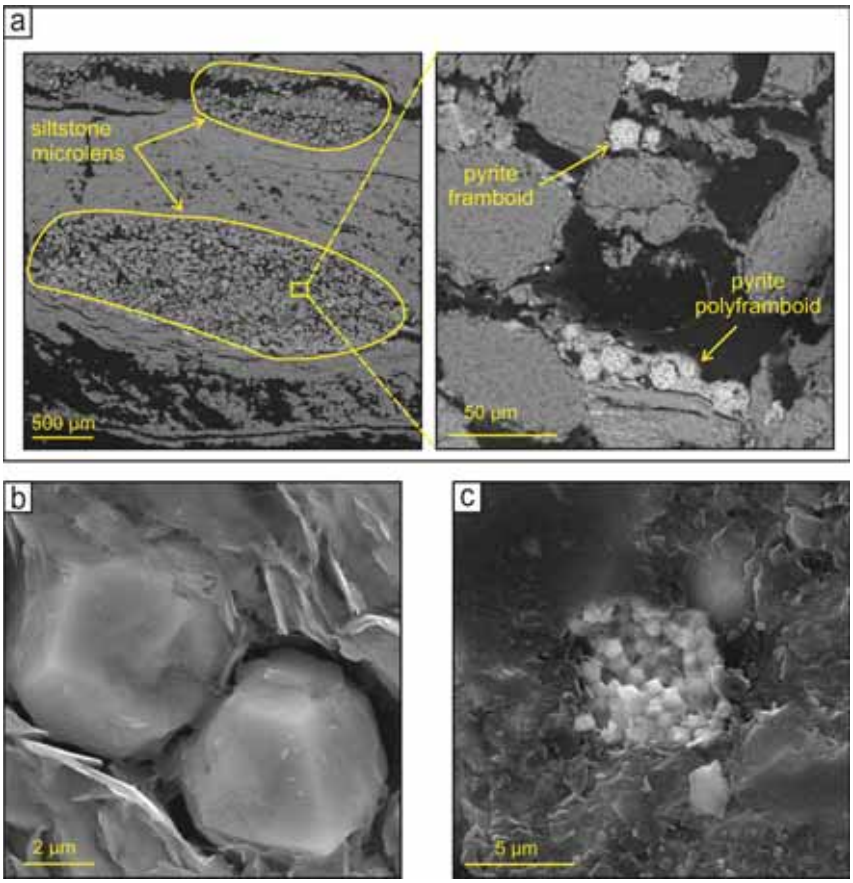

Figure 4. Pyrite textures in the studied sediments. (a) Siltstone microlens with pyrite framboids and polyframboids in Eocene claystone (sample 2). (b) Euhedral pyrite in Eocene claystone (sample 1). (c) Pyrite framboid in Paleocene sandstone (sample 40). The images are (a) backscattered and (b, c) secondary electron micrographs.

iron sulfide nodules (up to about 1 mm, Figures 5c–5f), which have variable shape, often with a spiky exterior surface (Figures 5c–5g), and consist of randomly oriented fine acicular pyrrhotite laths (Figures 5c, 5f, and 5i). Pyrrhotite sometimes occurs as growths within microcracks or cleavage planes in detrital silicate minerals (Figures 5g and 5h) or in spheroidal siderite (Figures 5c and 5d).

Ferrimagnetic iron sulfides in the Bakchar deposit are always associated with siderite across the P-E boundary. Siderite occurs as cement in the P-E deposits (Figure 6a), around amorphous Fe^{3+}, lepidocrocite (Figure 6b), chamosite matrix (Figure 6d), or chamosite-goethite ooliths (Figure 6c). Siderite is present at the base of the cemented oolitic ironstone in a chamosite-siderite (or lepidocrocite-siderite) cement with sphalerite (Figures 6d and 6e) and rarely with barite crystals (Figures 6b and 6f). Siderite is the main cement that occupies intergranular spaces at the top of the Paleocene ironstone and Eocene gritstone. It sometimes forms concretions in association with pyrrhotite (Figures 5c and 5d). Siderite microcrystals or aggregates (up to 50 μm diameter) sometimes occur with sphalerite (Figure 6h) and apatite (Figure 6i) in the chamosite cement (Figure 6g) of Maastrichtian deposits. Sphalerite occurs in spherical (Figure 6h) and, rarely, sudhedral (Figure 6e) shapes.

4.4. Geochemistry

The PETM is a 4.5 and 5.5 m thick interval within cores 803 (162.5–168.0 m) and 807 (167.5–173.0 m), respectively, that is clearly delineated by 0.6–2.2‰ negative excursions in bulk organic $\delta^{13}C$ (Figure 7 and Table A2). $\delta^{13}C_{org}$ values vary from −27.6‰ to −26.6‰ through the PETM, with TOC values up to 0.83% (Figure 7 and Table A2). The magnitude of bulk organic $\delta^{13}C$ values in the Bakchar deposit is comparable to

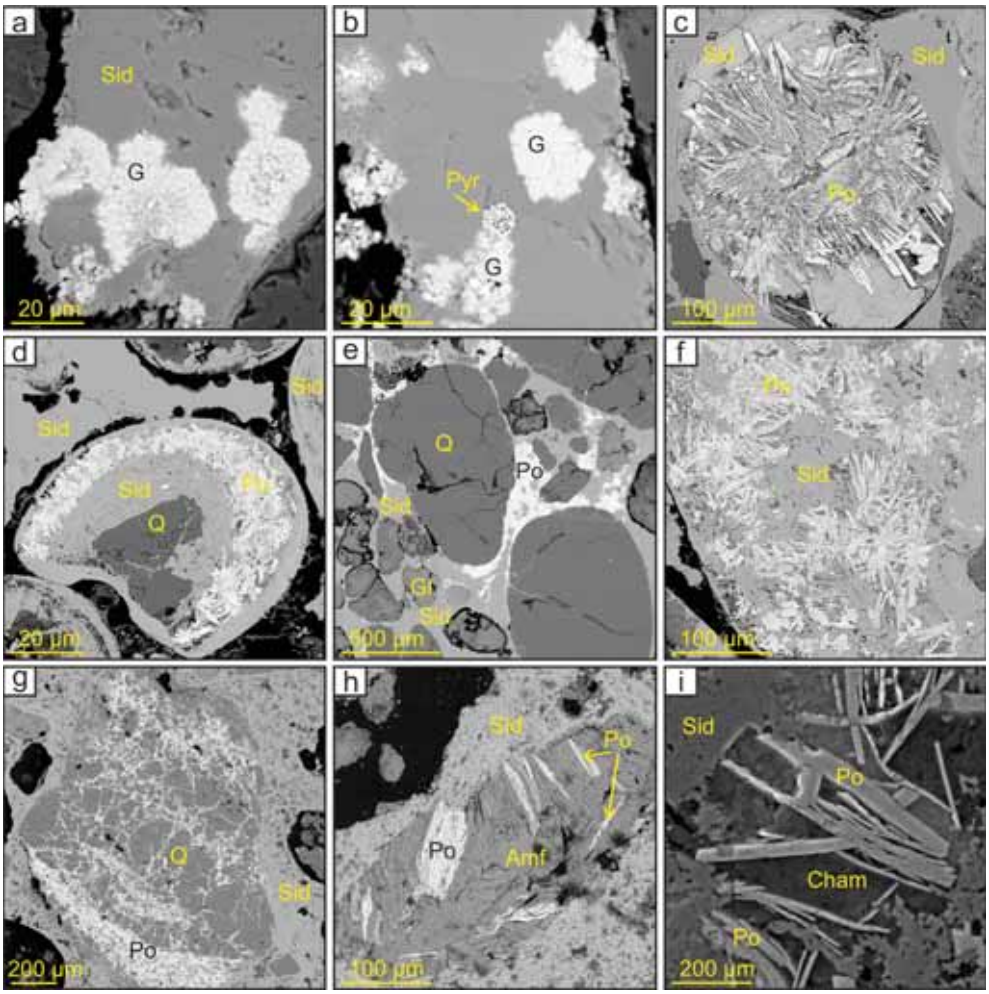

Figure 5. Magnetic iron sulfide textures in the studied sediments. (a) Greigite aggregate and (b) greigite with pyrite framboid in siderite cement within Eocene gritstone (both sample 3). (c and d) Pyrrhotite nodules within spheroidal siderite (both sample 31). (e and f) Pyrrhotite nodules in siderite matrix within Eocene gritstone (e, sample 3) and Paleocene oolitic ironstone (f, sample 31). (g and h) Pyrrhotite within (g) microcracks in detrital quartz and (h) cleavage planes in amphibole in oolitic ironstone (sample 31). (i) Fine acicular pyrrhotite laths in gritstone (sample 3). G, greigite; Po, pyrrhotite; Pyr, pyrite; Sid, siderite; Q, quartz; Gl, glauconite; Amf, amphibole; and Cham, chamosite cement. The images are (a–h) backscattered and (i) secondary electron micrographs.

those of marine carbon isotope excursions (CIEs) recorded elsewhere (1.5–5.1‰; Manners et al., 2013; McInerney & Wing, 2011). The stratigraphic distribution of trace element EFs and major elements are shown in Figure 7 and Table A3. These elements are usually considered as reliable proxies for estimating sedimentary oxygenation conditions (Mo, U, V) and primary productivity (Ba, Zn, Cu, P) in marine environments, and variation of clastic fluxes (Al, Ti) (Algeo & Tribovillard, 2009; Brumsack, 2006; Lebedel et al., 2013; Tribovillard et al., 2006). The average TOC content is 0.29 ± 0.19% (±standard deviation). However, sediments with pyrrhotite, greigite, and siderite within the PETM sequence from depths of 169 and 168 m have relatively high TOC values of 0.64% and 0.83%, respectively. Ti correlates with Al ($r > 0.75$), which indicates a siliciclastic origin with fluctuations that can be linked to detrital variations (Lebedel et al., 2013; Murphy et al., 2000; Rachold & Brumsack, 2001; Tribovillard et al., 2006). Other elements (Mo, U, V, Ba, Zn, Cu, P) have a biogenic or authigenic origin (Algeo & Maynard, 2004; Brumsack, 2006; Calvert & Pedersen, 1993; Lebedel et al., 2013; Morales et al., 2015; Riquier et al., 2006) because they are poorly correlated or uncorrelated with Al ($r < 0.6$). In the Upper Paleocene portion of the Bakchar section, EF values of redox proxies are relatively stable but high, ranging up to 15 for Mo, 18 for U, and 37 for V. Peak values coincide with oolitic ironstones with

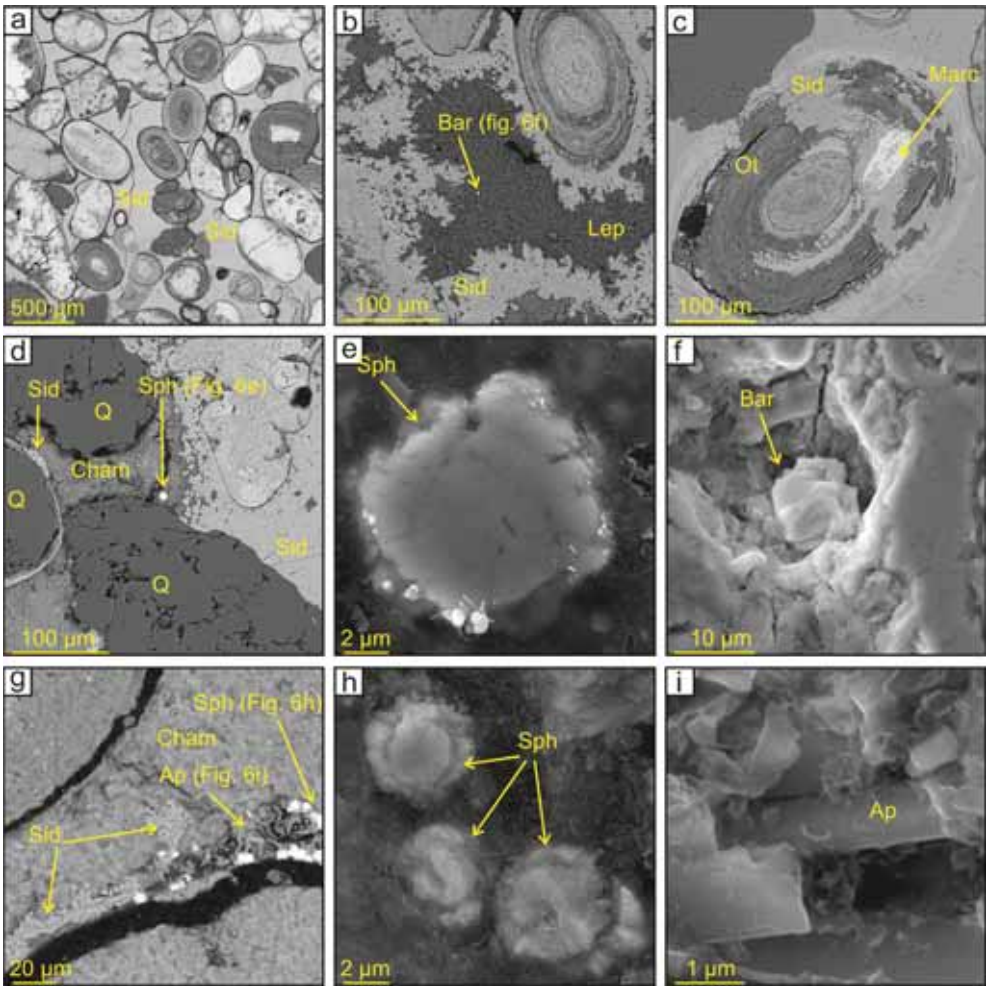

Figure 6. (a, b, c, d, g) Backscattered and (e, f, h, i) secondary electron micrographs of cementing minerals in the studied sediments. (a) Siderite matrix in Paleocene oolitic ironstone (sample 32). (b) Replacement of siderite by lepidocrocite with barite crystal (sample 33). (c) Replacement of chamosite-goethite oolith by formation of siderite and marcasite (sample 33). (d) Chamosite-siderite matrix with (e) subhedral sphalerite in Paleocene oolitic ironstone (sample 5). (f) Barite within lepidocrocite matrix (sample 33). (g) Chamosite matrix with siderite, (h) spheroidal sphalerite, and (i) apatite in Maastrichtian oolitic ironstone (sample 20). Sid, siderite; Ot, chamosite-goethite ooliths; Q, quartz; Cham, chamosite; Lep, lepidocrocite or amorphous Fe^{3+} matrix; Bar, barite; Marc, marcasite; Sph, sphalerite; and Ap, apatite.

siderite cement and ferrimagnetic iron sulfides. These proxies are correlated with EFs for P and Fe. EF values for P and Fe exceed 6, and range up to 30.9 for P and 33.95 for Fe.

Peak Ba_{bio} values, which correspond to the Maastrichtian and Lower Paleocene deposits, precede observed EF increases for the paleoredox proxies. The next Ba_{bio} peak is recorded in gritstones with ferrimagnetic iron sulfides and siderite cement at the P-E boundary, with concentrations up to 660 ppm. Enrichment of paleoproductivity proxies Zn and P is high with EFs >10 in the Lower-Middle Paleocene and the Middle-Upper Paleocene, respectively. The peak Zn EF (19.15) occurs in loose oolitic ironstone with low Ba_{bio} concentrations (18.41 ppm). EFs of Cu and Ti are low (<1 and ~1, respectively) in the studied section.

4.5. Fluid Inclusions

We selected only well-defined fluid inclusions from siderite for microthermometric analysis. Based on petrographic studies of fluid inclusions and their phase features at room temperature and phase transitions during heating and cooling, fluid inclusions occur in two types: Type A—two-phase (gas-liquid) inclusions and Type B—liquid-only inclusions. Type A inclusions are predominant (>80% of all

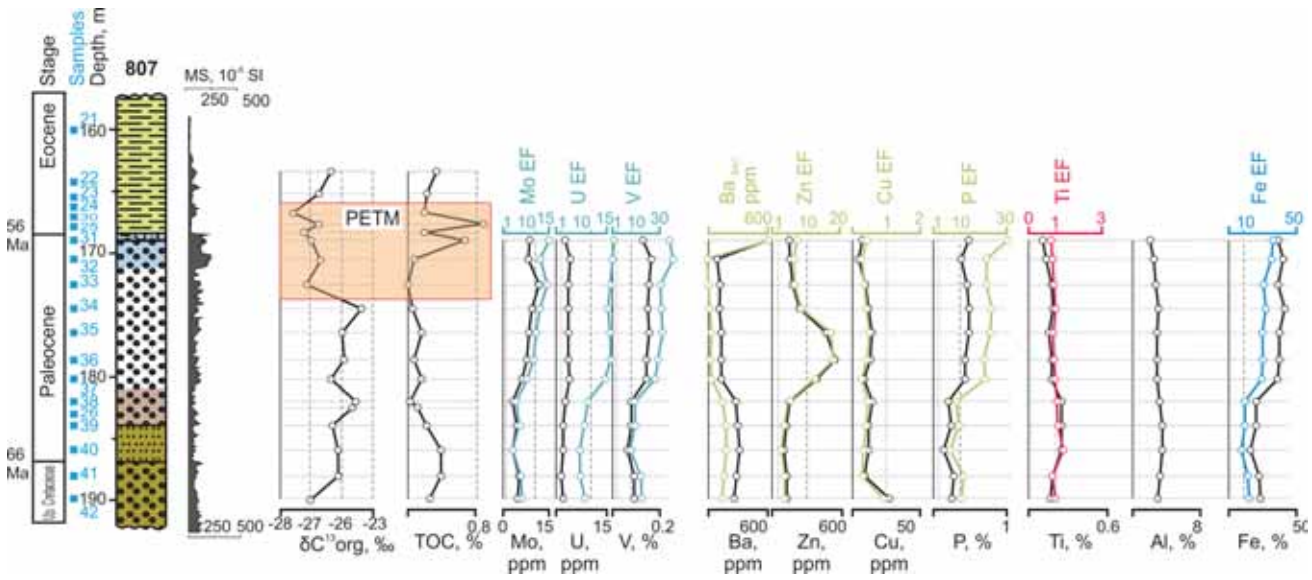

Figure 7. Stratigraphic column for hole 807 through the Bakchar deposit with geochemical profiles of $\delta^{13}C_{org}$, TOC, elemental enrichment factors (EFs), and Al content.

inclusions) and have diameters of mainly 2–6 μm (with a few reaching 6 μm), with round and elongated shapes, commonly with 10–40 vol % in the vapor phase, and mostly homogenize into a liquid phase. The ice melting temperature varied from +3°C to +6°C, which may be due to the presence of a clathrate phase (Bakker et al., 1996). The homogenization temperature is in the 165–290°C range with a bimodal distribution of 165°C to 171°C and 190°C to 290°C. Type B inclusions are usually round or ellipsoidal and 2–4 μm in size. Freezing and heating experiments of Type B inclusions were restricted due to the small size (mostly 2–3 μm) of inclusions. However, all Type B inclusions homogenize to the liquid phase upon heating. We used Raman spectroscopy to identify the composition of fluid inclusions, which consist of water and methane with subordinate ethane (Figure 8). Characteristic liquid phase peaks are located on a broad hump between 2,800 and 2,950 cm^{-1}. The sharp peak that shifts position at 2912.94 cm^{-1} is due to a methane inclusion (Frezzotti et al., 2012; Lu et al., 2008; Pironon et al., 1991).

5. Discussion

5.1. Distribution and Formation of Diagenetic Minerals

Authigenic siderite growth occurs during methanogenesis when ongoing iron reduction results in build-up of Fe^{2+} in interstitial waters when sulfide is no longer available and cannot react to form iron sulfides. If interstitial waters are saturated with respect to carbonate, Fe^{2+} will react with carbonate to form siderite. SEM observations indicate that siderite and iron sulfide formation occurred over more than one episode in the studied sediments. This might be related to different methane, for example, due to local biogenic methane or deeper thermogenic methane, which are difficult to distinguish between with available data. In some cases, siderite has clearly overgrown early diagenetic iron sulfides (Figures 5a and 5b), while in other cases pyrrhotite has overgrown siderite, and has then been overgrown by later siderite (Figure 5d). This indicates progressive growth of iron sulfide and siderite during diagenesis. Greigite and pyrrhotite formation requires dissolved sulfide, which is produced by consortia of sulfate-reducing bacteria and methanotrophic archaea in marine sediments (Boetius et al., 2000) that cause pore waters to become sulfidic in association with anaerobic oxidation of methane. The released sulfide then reacts with Fe^{2+}-rich siderite and remaining iron-bearing minerals to form iron sulfide (Jørgensen et al., 2004;

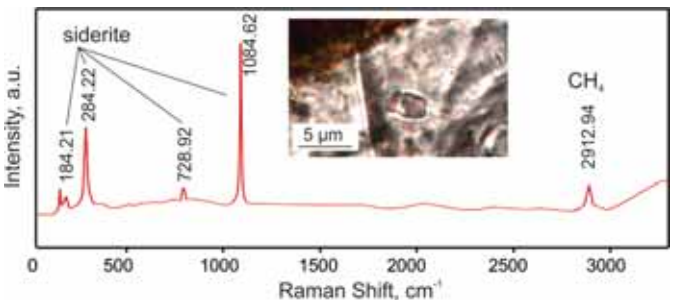

Figure 8. Laser Raman spectrum collected from pure methane inclusions within siderite cement (sample 4). The inset is an optical photomicrograph taken under transmitted light.

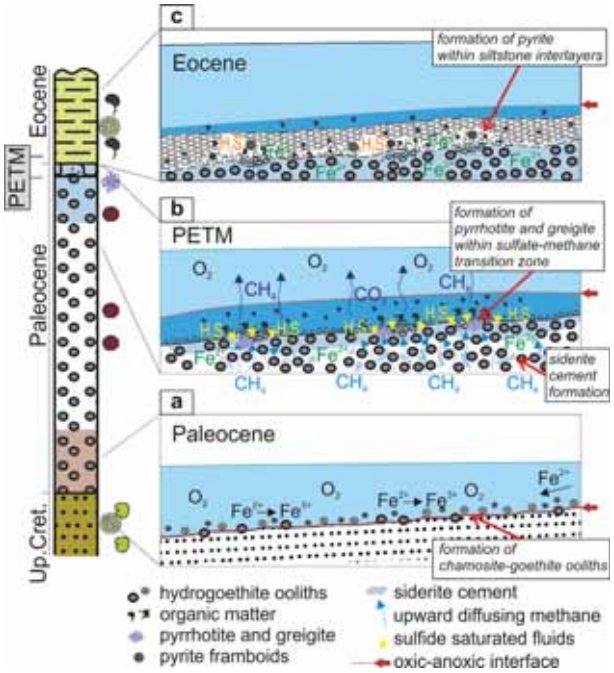

Figure 9. Proposed model for environmental conditions during deposition of the Paleocene-Eocene Bakchar sequence. (a) Chamosite-goethite ooliths and ooids formation under oxic conditions at the sediment-water interface during the Paleocene (pre-PETM). (b) Upward methane diffusion through sediment pore spaces. Reaction of CO_2 with Fe^{2+} will form siderite cement (PETM), with anaerobic oxidation of methane producing sulfide and enabling pyrrhotite and greigite formation at the sulfate-methane transition zone. (c) With continued claystone and interlayered siltstone deposition, ongoing organic matter degradation gave rise to pyrite framboid formation within siltstone interlayers (post-PETM).

Kasten et al., 1998; Larrasoaña et al., 2007; Neretin et al., 2004; Riedinger et al., 2005; Roberts & Weaver, 2005). A close association of greigite and pyrrhotite with siderite is indicative of methanogenesis and sulfate reduction in marine diagenetic environments (Jørgensen & Kasten, 2006; Larrasoaña et al., 2007). The presence of methane fluid inclusions in siderite cement (Figure 8) within the studied oolitic ironstone and gritstone confirms this interpretation. Framboidal greigite and pyrite form during early burial (Berner, 1981).

Siderite cement in the oolitic ironstones contains minerals (goethite, hydrogoethite) that formed under oxic conditions. Ooids generally form in warm, carbonate supersaturated, shallow marine intertidal environments where small sediment particles act as a "seed" onto which calcite precipitates. Ooids grow as they are washed around the seabed by strong intertidal currents. The abundance of Fe^{3+}-oxides in the oolites indicates that they formed in an oxic depositional environment, which is consistent with oolith formation in active intertidal environments (Figure 9a). In contrast, siderite cement will have formed in a methanic, nonsulfidic diagenetic environment in which dissolved Fe^{2+} reacted in carbonate-saturated marine pore waters (Berner, 1981; Mücke, 2006; Roberts, 2015). This indicates that the sediments underwent a marked change in diagenetic environment from oxic to methanic (Figures 9a and 9b). Changes in diagenetic environment of the type observed are caused by progressive microbial decomposition of organic matter (Boetius & Wenzhöfer, 2013; Danise et al., 2012). The chamosite-goethite aggregates that formed under oxic conditions (as ooliths and ooids) remain stable under methanic conditions (Berner, 1969, 1981; Froelich et al., 1979). However, iron oxides and hydroxides are highly reactive under sulfidic diagenetic conditions (Roberts, 2015). The lack of oolith bleaching indicates that even though the sediments experienced sulfidic diagenesis, as indicated by the presence of early diagenetic iron sulfides, they were either protected from reaction by a tight carbonate cement or they were not exposed to sulfidic pore waters for long enough for these minerals to have undergone dissolution. Such a scenario would have required a rapid environmental change that shifted the diagenetic environment from oxic to methanic with little time spent under sulfidic conditions. This is possible with sudden methane diffusion and/or increase in marine productivity associated with the PETM (Figure 7). In some cases, siderite has replaced chamosite-goethite ooliths (Figure 6c). This appears to have been rare probably because there was sufficient amorphous Fe^{3+} and lepidocrocite in the sedimentary environment to be reduced and react with CO_2 to form iron carbonate. Alternatively, siderite formation could have arisen directly from amorphous Fe^{3+} and lepidocrocite (Figure 6b), which are the most reactive iron minerals used by bacteria as electron acceptors (Lovley & Phillips, 1986; Munch & Ottow, 1983; Sivan et al., 2016). Primary formation of these minerals within the studied iron-bearing sediments (Figure 3c) could have limited oolith bleaching. Fe^{3+}-oxide minerals could have played an important role as natural electrodes to create syntrophic interactions that facilitated methane production (Egger et al., 2016, 2017; Jiang et al., 2013; Kato et al., 2012; Sivan et al., 2016). We favor a hypothesis involving sudden environmental change from oxic to methanic to explain preservation of Fe^{3+}-bearing minerals within otherwise reducing diagenetic environments. A similar argument concerning a rapid change to ferruginous diagenetic conditions during periods with high-CO_2 environments has been proposed to explain magnetite magnetofossil preservation in PETM clays on the mid-Atlantic North American margin (Kopp et al., 2009).

Three main factors contributed to pyrrhotite and greigite formation in Paleocene oolitic ironstones and Eocene gritstones (Figure 9b): methane diffusion, anaerobic oxidation of methane, and limited bacterial sulfate reduction. Pyrrhotite occurs in both siderite nodules (Figures 5c and 5d) and siderite cement (Figures 5e and 5f), and is likely to have formed via reaction with limited sulfide produced during anaerobic oxidation of methane. CO_2 and sulfide-saturated fluids appear to have penetrated interstitial spaces and

microcracks in detrital grains (Figure 5g), which gave rise to siderite and pyrrhotite formation around and inside detrital mineral grains. Pyrrhotite and greigite have been described in other marine sediments where concentration gradients of methane occur near disseminated gas hydrates (Jørgensen et al., 2004; Kars & Kodama, 2015a, 2015b; Neretin et al., 2004; Roberts et al., 2010). Formation of sphalerite in the studied Paleocene oolitic ironstones may also have been associated with localized bacterial sulfate reduction and HS^- release. This sulfide reacted with Zn (Labrenz et al., 2000; Tribovillard et al., 2006) to form sphalerite, whereas dissolved Fe^{2+} reacted with CO_2 to form siderite cement.

The presence of pyrite and the absence of ferrimagnetic iron sulfides in the overlying Eocene claystones and underlying Upper Cretaceous deposits (Figure 4) is explained by completion of pyritization reactions associated with bacterial sulfate reduction (Berner, 1984; Lin et al., 2016; Núñez-Useche et al., 2016; Wei et al., 2015). Likewise, formation of ferrimagnetic iron sulfides only within the PETM interval provides strong evidence that their formation was associated with environmental conditions during the PETM and not during subsequent burial.

5.2. Paleoredox Change and Possible Methane Source

The bimodal distribution of fluid inclusion homogenization temperatures in siderite indicates that fluids in the Bakchar deposit could have had two different sources (due to local biogenic and/or deep thermogenic methane production). As argued below, the evidence favors a biogenic origin, but we do not have sufficient data to argue strongly either way. Progressive siderite and iron sulfide formation in more than one episode within the Paleocene oolitic ironstones may indicate ongoing upward methane diffusion through sediment pore spaces via methane microseepage (Figure 9b) (Etiope & Klusman, 2002; Kvenvolden & Rogers, 2005). The methane would then have undergone anaerobic oxidation that produced reactants that interacted with iron-bearing minerals and dissolved Fe^{2+} to form iron sulfides. Preservation of water and methane in fluid inclusions within siderite cement with homogenization temperatures of 190–290°C was probably linked to biogenic methane (i.e., gas-condensate) migration through the sediment (e.g., Schubert et al., 2007), where gas-condensates consist of heterogeneous mixtures of CO_2, H_2S, and CH_4-rich gas, hydrocarbons, and water. Some part of the upward diffusing methane could have been released through the water column to the atmosphere (e.g., Westbrook et al., 2009), and might have played a role in driving global climate change across the PETM (Carozza et al., 2011; Yamamoto et al., 2009).

Further evidence concerning the diagenetic environments of the P-E Bakchar deposit is provided by geochemical results. High enrichment of Mo, U, and V with weak background Cu enrichment in the Paleocene ironstones reflect reducing postdepositional environmental conditions with little organic matter (Brumsack, 2006; Lebedel et al., 2013; Tribovillard et al., 2006, 2012). The absence of pyrite and a predominantly siderite matrix were probably linked to upward diffusing methanic fluids. The increased TOC content in the upper part of the studied oolitic ironstones is likely to have been associated with methanic siderite-forming conditions across the PETM. Local sulfidization is evident from minor sphalerite formation in the Paleocene oolitic ironstones with chamosite-siderite matrix. The Zn that contributed to sphalerite formation was probably adsorbed from sea water onto iron-oxyhydroxide particles, and was then released from organometallic complexes in sulfidic postdepositional pore waters (Tribovillard et al., 2006; Labrenz et al., 2000). All of the above evidence indicates that marine sulfidic environments dominated below the seafloor of the Western Siberia Sea across the PETM under the influence of significant methane emissions, and locally increased paleoproductivity. Sulfidic diagenetic activity lasted for a relatively short period of time through the PETM, after which pelitic marine sediments accumulated under stagnant bottom waters (Figure 9c) where pyrite formation occurred without preservation of ferrimagnetic iron sulfides. The association of diagenetic minerals (e.g., siderite, barite, and apatite) with the PETM interval, indications of increased paleoproductivity across the PETM, temperature homogenization of fluid inclusions in siderite, bulk organic $\delta^{13}C$ results, and the presence of ferrimagnetic iron sulfides in the PETM section, are all consistent with observations from modern environments associated with gas hydrate dissociation (e.g., Kars & Kodama, 2015a, 2015b; Larrasoaña et al., 2007) and provide evidence for a biogenic methane source (Dickens, 2011; Dickens et al., 1995, 1997; Panchuk et al., 2008; Zeebe, 2013).

Given that the studied sediments are largely unlithified (lithification is enhanced in places by chemical precipitation rather than by burial compaction), and that the overlying and underlying sediments were deposited under oxic conditions that did not undergo later sulfidic diagenesis, authigenic mineral formation associated with methane venting as identified in this study is interpreted to have been associated only with

the PETM. The accepted best estimate of the total duration of the PETM is about 170,000 years (Röhl et al., 2007). Based on a 5 m thickness, the sedimentation rate through the studied PETM interval averages ~3 cm/kyr. Iron sulfides and iron carbonates can form over short periods of days to years, so there was abundant time for the observed minerals to have formed during the PETM. Overall, the PETM was a relatively short-lived event during which enhanced organic carbon productivity and preservation drove early diagenetic conditions in the Bakchar deposit rapidly from oxic into methanic conditions.

5.3. Paleoclimatic Implications and Magnetic Identification of Pyrrhotite and Greigite

Anaerobic oxidation of methane combined with microbial sulfate reduction were the most important processes that contributed to authigenic mineral formation in PETM sediments of the epicontinental West Siberian Sea. The main factors that influence these processes are the amount of organic matter, which was driven by biological productivity in the basin, bottom water and sedimentary oxygenation, pore water chemistry, sediment grain size (porosity and permeability), and sedimentation rate. In the studied sediments, greigite and pyrrhotite formation were evidently linked to upward methane diffusion and sulfide limitation (e.g., Larrasoaña et al., 2007). The presence of methane within fluid inclusions in the studied sediments provides rare direct evidence for methane mobilization that is relevant to one of the major hypotheses concerning the cause of the PETM. Thus, while there is no compelling evidence to link local methane venting across the PETM in the West Siberian Sea with more widespread methane mobilization and global warming, the magnetic, petrographic, and geochemical approach used here should be applicable to identifying authigenic minerals that provide telltale signatures of methane mobility that can be used to study the PETM and other events. Such analyses could prove crucial for assessing whether methane emissions played a decisive role in driving global warming across the PETM (Carozza et al., 2011; Lourens et al., 2005; Stassen et al., 2015; Thomas et al., 2002; Yamamoto et al., 2009).

Pyrrhotite and greigite formation in the Bakchar oolitic ironstones and gritstones have produced high magnetic susceptibilities in these rocks. These ferrimagnetic iron sulfides were recognized based on sediment magnetic susceptibility (Figure 2) values $>80 \times 10^{-5}$ SI (140.5–232.8 $\times 10^{-5}$ SI, first and third quartiles). While such values are not unique to sediments that contain these minerals, magnetic susceptibility analyses could provide a useful first indication of the presence of these minerals from similar ancient environments. Regardless, identification of diagenetic greigite and pyrrhotite that formed in association with methanogenesis should help to assess the role of ancient methane hydrate migrations in sedimentary deposits.

6. Conclusions

Based on lithological, mineralogical, magnetic susceptibility, and geochemical analysis of the PETM Bakchar deposit from the West Siberian Sea, we demonstrate that the studied sediments contain ferrimagnetic iron sulfide minerals associated with siderite cement that provide evidence of ancient methane migration. This conclusion is confirmed by the presence of methane within fluid inclusions from the siderite cement. Methane migration associated with ancient methane hydrate dissociation is one possible option, followed by its escape to the atmosphere, for explaining the marked global warming and carbon isotope excursion associated with the PETM (e.g., Dickens et al., 1995). While detection of methane venting within a single stratigraphic sequence does not enable testing of this hypothesis, documentation of the presence of authigenic iron sulfides and siderite produced via diagenetic fluid-rock reactions provides a key means of assessing whether methane venting has occurred within an ancient sedimentary sequence. We suggest that documentation of the presence of pyrrhotite and greigite that resulted from anaerobic oxidation of methane, such as in the studied Bakchar deposit, should become a useful tool for routine detection of ancient methane hydrate migration in sedimentary rocks.

Appendix

This appendix provides all the data, which has been used in this paper. It includes the data (Table A1) to generate magnetic susceptibility profiles in Figures 1 and 7, and the organic geochemistry data (Table A2) to create the carbon isotope excursions and the total organic carbon profile in Figure 7. It also includes the geochemistry data (Table A3) to analyze paleoenvironmental conditions and to generate geochemical profiles in Figure 7.

Table A1
Magnetic Susceptibility (MS) Values Across the PETM Interval of the Bakchar Section

Depth (m)			Depth (m)			Depth (m)		
From	To	MS × 10^{-5} SI	From	To	MS × 10^{-5} SI	From	To	MS × 10^{-5} SI
Drill hole 803								
155.1	155.2	15.5	159.1	159.2	38.6	163.1	163.2	30.8
155.2	155.3	15.4	159.2	159.3	101.7	163.2	163.3	33.5
155.3	155.4	19.2	159.3	159.4	57.6	163.3	163.4	167.8
155.4	155.5	22.6	159.4	159.5	83.5	163.4	163.5	289.2
155.5	155.6	27.7	159.5	159.6	135.2	163.5	163.6	183.9
155.6	155.7	18.5	159.6	159.7	110.4	163.6	163.7	181.1
155.7	155.8	14.3	159.7	159.8	47.5	163.7	163.8	181.0
155.8	155.9	16.0	159.8	159.9	62.0	163.8	163.9	143.3
155.9	156.0	15.3	159.9	160.0	108.0	163.9	164.0	116.2
156.0	156.1	10.5	160.0	160.1	73.0	164.0	164.1	201.3
156.1	156.2	8.5	160.1	160.2	51.5	164.1	164.2	179.4
156.2	156.3	13.9	160.2	160.3	55.8	164.2	164.3	205.1
156.3	156.4	16.7	160.3	160.4	54.6	164.3	164.4	151.0
156.4	156.5	16.8	160.4	160.5	58.0	164.4	164.5	164.3
156.5	156.6	18.8	160.5	160.6	40.9	164.5	164.6	218.3
156.6	156.7	20.2	160.6	160.7	30.3	164.6	164.7	187.8
156.7	156.8	21.9	160.7	160.8	24.1	164.7	164.8	207.9
156.8	156.9	26.5	160.8	160.9	23.9	164.8	164.9	145.7
156.9	157.0	36.4	160.9	161.0	20.7	164.9	165.0	152.9
157.0	157.1	37.8	161.0	161.1	30.4	165.0	165.1	178.2
157.1	157.2	27.4	161.1	161.2	36.8	165.1	165.2	175.7
157.2	157.3	49.0	161.2	161.3	35.5	165.2	165.3	172.2
157.3	157.4	50.9	161.3	161.4	165.4	165.3	165.4	184.0
157.4	157.5	50.5	161.4	161.5	128.8	165.4	165.5	140.4
157.5	157.6	46.7	161.5	161.6	24.3	165.5	165.6	125.9
157.6	157.7	49.9	161.6	161.7	24.4	165.6	165.7	132.1
157.7	157.8	57.8	161.7	161.8	22.1	165.7	165.8	117.8
157.8	157.9	48.5	161.8	161.9	27.6	165.8	165.9	144.1
157.9	158.0	47.7	161.9	162.0	26.4	165.9	166.0	125.5
158.0	158.1	56.4	162.0	162.1	28.5	166.0	166.1	106.6
158.1	158.2	148.9	162.1	162.2	17.7	166.1	166.2	118.2
158.2	158.3	155.8	162.2	162.3	13.9	166.2	166.3	155.5
158.3	158.4	88.0	162.3	162.4	19.3	166.3	166.4	146.8
158.4	158.5	58.6	162.4	162.5	24.4	166.4	166.5	183.0
158.5	158.6	46.3	162.5	162.6	21.6	166.5	166.6	136.5
158.6	158.7	57.5	162.6	162.7	20.1	166.6	166.7	118.8
158.7	158.8	49.6	162.7	162.8	20.8	166.7	166.8	164.5
158.8	158.9	45.4	162.8	162.9	23.1	166.8	166.9	168.9
158.9	159.0	35.0	162.9	163.0	29.0	166.9	167.0	119.5
159.0	159.1	28.7	163.0	163.1	30.0	167.0	167.1	132.1
167.1	167.2	116.0	171.1	171.2	102.6	175.1	175.2	32.7
167.2	167.3	145.1	171.2	171.3	90.6	175.2	175.3	39.3
167.3	167.4	130.3	171.3	171.4	80.3	175.3	175.4	69.3
167.4	167.5	78.2	171.4	171.5	80.7	175.4	175.5	68.7
167.5	167.6	136.3	171.5	171.6	51.4	175.5	175.6	69.8
167.6	167.7	129.1	171.6	171.7	58.8	175.6	175.7	67.3
167.7	167.8	126.7	171.7	171.8	53.7	175.7	175.8	65.7
167.8	167.9	86.5	171.8	171.9	50.7	175.8	175.9	71.0
167.9	168.0	60.6	171.9	172.0	56.9	175.9	176.0	60.8
168.0	168.1	63.6	172.0	172.1	42.7	176.0	176.1	54.7
168.1	168.2	45.6	172.1	172.2	35.0	176.1	176.2	33.6
168.2	168.3	60.6	172.2	172.3	57.0	176.2	176.3	32.9
168.3	168.4	51.3	172.3	172.4	62.6	176.3	176.4	39.2
168.4	168.5	52.6	172.4	172.5	53.4	176.4	176.5	53.3

Table A1. (continued)

Depth (m)			Depth (m)			Depth (m)		
From	To	MS × 10^{-5} SI	From	To	MS × 10^{-5} SI	From	To	MS × 10^{-5} SI
168.5	168.6	50.3	172.5	172.6	71.7	176.5	176.6	51.8
168.6	168.7	44.7	172.6	172.7	64.2	176.6	176.7	44.4
168.7	168.8	37.1	172.7	172.8	65.9	176.7	176.8	28.6
168.8	168.9	36.5	172.8	172.9	69.3	176.8	176.9	35.1
168.9	169.0	54.7	172.9	173.0	59.8	176.9	177.0	42.4
169.0	169.1	44.7	173.0	173.1	63.3	177.0	177.1	41.2
169.1	169.2	50.1	173.1	173.2	119.8	177.1	177.2	56.0
169.2	169.3	34.1	173.2	173.3	59.7	177.2	177.3	52.1
169.3	169.4	30.8	173.3	173.4	62.5	177.3	177.4	50.8
169.4	169.5	27.7	173.4	173.5	62.9	177.4	177.5	49.9
169.5	169.6	32.3	173.5	173.6	66.4	177.5	177.6	56.0
169.6	169.7	28.9	173.6	173.7	38.9	177.6	177.7	65.2
169.7	169.8	33.0	173.7	173.8	33.6	177.7	177.8	41.5
169.8	169.9	27.5	173.8	173.9	64.4	177.8	177.9	38.3
169.9	170.0	26.4	173.9	174.0	43.9	177.9	178.0	50.1
170.0	170.1	34.4	174.0	174.1	36.6	178.0	178.1	36.6
170.1	170.2	41.9	174.1	174.2	58.1	178.1	178.2	36.0
170.2	170.3	37.8	174.2	174.3	44.3	178.2	178.3	27.8
170.3	170.4	55.4	174.3	174.4	54.2	178.3	178.4	24.6
170.4	170.5	63.9	174.4	174.5	80.7	178.4	178.5	29.8
170.5	170.6	39.3	174.5	174.6	61.5	178.5	178.6	33.7
170.6	170.7	40.7	174.6	174.7	54.1	178.6	178.7	35.9
170.7	170.8	53.1	174.7	174.8	55.0	178.7	178.8	37.6
170.8	170.9	57.0	174.8	174.9	71.0	178.8	178.9	26.1
170.9	171.0	59.1	174.9	175.0	59.2	178.9	179.0	37.9
171.0	171.1	41.9	175.0	175.1	47.3	179.0	179.1	39.7
179.1	179.2	63.2	182.0	182.1	28.9	184.9	185.0	35.8
179.2	179.3	31.2	182.1	182.2	30.5	185.0	185.1	42.1
179.3	179.4	32.9	182.2	182.3	20.1	185.1	185.2	82.3
179.4	179.5	30.1	182.3	182.4	25.3	185.2	185.3	53.9
179.5	179.6	30.5	182.4	182.5	37.3	185.3	185.4	31.8
179.6	179.7	22.4	182.5	182.6	11.5	185.4	185.5	80.2
179.7	179.8	38.3	182.6	182.7	32.2	185.5	185.6	76.6
179.8	179.9	24.3	182.7	182.8	38.4	185.6	185.7	43.3
179.9	180.0	19.6	182.8	182.9	40.7	185.7	185.8	37.5
180.0	180.1	30.8	182.9	183.0	27.4	185.8	185.9	38.7
180.1	180.2	22.1	183.0	183.1	27.7	185.9	186.0	37.1
180.2	180.3	20.2	183.1	183.2	31.6	186.0	186.1	38.7
180.3	180.4	37.4	183.2	183.3	22.0	186.1	186.2	40.0
180.4	180.5	21.5	183.3	183.4	17.3	186.2	186.3	39.7
180.5	180.6	16.3	183.4	183.5	32.5	186.3	186.4	53.0
180.6	180.7	25.5	183.5	183.6	31.1	186.4	186.5	47.7
180.7	180.8	26.6	183.6	183.7	41.8	186.5	186.6	58.8
180.8	180.9	36.5	183.7	183.8	66.1	186.6	186.7	31.0
180.9	181.0	25.6	183.8	183.9	54.0	186.7	186.8	30.2
181.0	181.1	27.0	183.9	184.0	52.6	186.8	186.9	48.7
181.1	181.2	24.2	184.0	184.1	48.1	186.9	187.0	69.7
181.2	181.3	43.0	184.1	184.2	51.0	187.0	187.1	56.1
181.3	181.4	30.8	184.2	184.3	27.3	187.1	187.2	40.0
181.4	181.5	22.4	184.3	184.4	22.1	187.2	187.3	62.4
181.5	181.6	20.8	184.4	184.5	51.0	187.3	187.4	54.3
181.6	181.7	46.6	184.5	184.6	43.1	187.4	187.5	38.4
181.7	181.8	30.8	184.6	184.7	41.6	187.5	187.6	62.0
181.8	181.9	43.4	184.7	184.8	33.3	187.6	187.7	69.8
181.9	182.0	40.2	184.8	184.9	36.0			
Drill hole 807								
155.1	155.2	30.0	156.1	156.2	11.6	157.1	157.2	5.7
155.2	155.3	31.0	156.2	156.3	4.5	157.2	157.3	17.0

Table A1. (continued)

Depth (m)			Depth (m)			Depth (m)		
From	To	MS × 10^{-5} SI	From	To	MS × 10^{-5} SI	From	To	MS × 10^{-5} SI
155.3	155.4	31.0	156.3	156.4	3.1	157.3	157.4	21.9
155.4	155.5	36.0	156.4	156.5	7.4	157.4	157.5	17.1
155.5	155.6	20.7	156.5	156.6	8.9	157.5	157.6	17.8
155.6	155.7	14.7	156.6	156.7	6.3	157.6	157.7	14.3
155.7	155.8	25.1	156.7	156.8	8.3	157.7	157.8	11.0
155.8	155.9	28.0	156.8	156.9	8.1	157.8	157.9	26.3
155.9	156.0	18.6	156.9	157.0	13.1	157.9	158.0	26.0
156.0	156.1	14.0	157.0	157.1	6.7	158.0	158.1	20.8
158.1	158.2	12.0	162.1	162.2	21.8	166.1	166.2	56.3
158.2	158.3	10.0	162.2	162.3	22.6	166.2	166.3	41.4
158.3	158.4	13.5	162.3	162.4	35.9	166.3	166.4	49.3
158.4	158.5	11.4	162.4	162.5	34.4	166.4	166.5	84.6
158.5	158.6	10.1	162.5	162.6	23.5	166.5	166.6	66.5
158.6	158.7	11.5	162.6	162.7	39.3	166.6	166.7	40.0
158.7	158.8	8.9	162.7	162.8	29.0	166.7	166.8	57.5
158.8	158.9	6.1	162.8	162.9	16.4	166.8	166.9	66.9
158.9	159.0	7.5	162.9	163.0	16.2	166.9	167.0	41.7
159.0	159.1	4.1	163.0	163.1	20.5	167.0	167.1	51.8
159.1	159.2	10.3	163.1	163.2	31.9	167.1	167.2	23.1
159.2	159.3	12.3	163.2	163.3	47.7	167.2	167.3	17.3
159.3	159.4	11.7	163.3	163.4	39.6	167.3	167.4	19.6
159.4	159.5	7.6	163.4	163.5	58.4	167.4	167.5	23.6
159.5	159.6	5.0	163.5	163.6	69.2	167.5	167.6	24.2
159.6	159.7	4.1	163.6	163.7	39.2	167.6	167.7	24.0
159.7	159.8	6.2	163.7	163.8	48.0	167.7	167.8	24.8
159.8	159.9	4.8	163.8	163.9	55.2	167.8	167.9	10.6
159.9	160.0	5.0	163.9	164.0	36.7	167.9	168.0	22.0
160.0	160.1	5.0	164.0	164.1	30.2	168.0	168.1	12.8
160.1	160.2	5.9	164.1	164.2	33.2	168.1	168.2	16.7
160.2	160.3	5.4	164.2	164.3	26.3	168.2	168.3	17.5
160.3	160.4	6.1	164.3	164.4	21.3	168.3	168.4	15.5
160.4	160.5	6.6	164.4	164.5	7.5	168.4	168.5	32.0
160.5	160.6	6.9	164.5	164.6	66.4	168.5	168.6	156.1
160.6	160.7	6.7	164.6	164.7	45.3	168.6	168.7	138.9
160.7	160.8	7.2	164.7	164.8	99.0	168.7	168.8	111.2
160.8	160.9	7.6	164.8	164.9	65.9	168.8	168.9	97.0
160.9	161.0	7.2	164.9	165.0	36.5	168.9	169.0	144.1
161.0	161.1	6.0	165.0	165.1	40.0	169.0	169.1	64.6
161.1	161.2	4.3	165.1	165.2	28.1	169.1	169.2	148.6
161.2	161.3	3.7	165.2	165.3	17.4	169.2	169.3	123.0
161.3	161.4	4.1	165.3	165.4	36.5	169.3	169.4	119.4
161.4	161.5	4.3	165.4	165.5	29.6	169.4	169.5	128.9
161.5	161.6	2.9	165.5	165.6	30.4	169.5	169.6	117.4
161.6	161.7	3.5	165.6	165.7	31.9	169.6	169.7	115.9
161.7	161.8	4.0	165.7	165.8	21.5	169.7	169.8	112.7
161.8	161.9	4.7	165.8	165.9	29.3	169.8	169.9	115.9
161.9	162.0	4.7	165.9	166.0	27.2	169.9	170.0	105.5
162.0	162.1	21.5	166.0	166.1	27.4	170.0	170.1	98.7
170.1	170.2	124.3	174.1	174.2	119.7	178.1	178.2	50.7
170.2	170.3	186.4	174.2	174.3	111.5	178.2	178.3	31.8
170.3	170.4	184.1	174.3	174.4	55.4	178.3	178.4	25.0
170.4	170.5	172.9	174.4	174.5	71.1	178.4	178.5	44.8
170.5	170.6	185.1	174.5	174.6	69.6	178.5	178.6	79.6
170.6	170.7	171.9	174.6	174.7	79.1	178.6	178.7	82.1
170.7	170.8	139.4	174.7	174.8	84.7	178.7	178.8	73.8
170.8	170.9	162.5	174.8	174.9	73.2	178.8	178.9	51.6
170.9	171.0	155.9	174.9	175.0	54.8	178.9	179.0	73.4
171.0	171.1	147.5	175.0	175.1	38.2	179.0	179.1	55.8

Table A1. (continued)

Depth (m)			Depth (m)			Depth (m)		
From	To	MS × 10^{-5} SI	From	To	MS × 10^{-5} SI	From	To	MS × 10^{-5} SI
171.1	171.2	148.3	175.1	175.2	25.4	179.1	179.2	52.8
171.2	171.3	116.5	175.2	175.3	45.8	179.2	179.3	27.1
171.3	171.4	56.3	175.3	175.4	104.7	179.3	179.4	82.4
171.4	171.5	53.5	175.4	175.5	73.0	179.4	179.5	63.8
171.5	171.6	49.3	175.5	175.6	64.6	179.5	179.6	63.2
171.6	171.7	40.5	175.6	175.7	83.7	179.6	179.7	67.3
171.7	171.8	64.5	175.7	175.8	78.6	179.7	179.8	81.6
171.8	171.9	81.7	175.8	175.9	64.0	179.8	179.9	89.0
171.9	172.0	51.7	175.9	176.0	77.3	179.9	180.0	95.7
172.0	172.1	32.4	176.0	176.1	74.4	180.0	180.1	71.9
172.1	172.2	35.8	176.1	176.2	83.6	180.1	180.2	56.7
172.2	172.3	45.9	176.2	176.3	100.6	180.2	180.3	76.9
172.3	172.4	53.1	176.3	176.4	88.8	180.3	180.4	89.7
172.4	172.5	97.2	176.4	176.5	70.9	180.4	180.5	94.2
172.5	172.6	94.4	176.5	176.6	71.8	180.5	180.6	86.0
172.6	172.7	94.8	176.6	176.7	64.1	180.6	180.7	74.8
172.7	172.8	99.0	176.7	176.8	45.8	180.7	180.8	53.1
172.8	172.9	57.4	176.8	176.9	50.0	180.8	180.9	47.9
172.9	173.0	75.6	176.9	177.0	40.3	180.9	181.0	36.3
173.0	173.1	99.4	177.0	177.1	22.6	181.0	181.1	51.4
173.1	173.2	119.6	177.1	177.2	49.0	181.1	181.2	27.2
173.2	173.3	105.7	177.2	177.3	51.3	181.2	181.3	44.3
173.3	173.4	79.2	177.3	177.4	72.0	181.3	181.4	37.9
173.4	173.5	66.6	177.4	177.5	62.7	181.4	181.5	18.2
173.5	173.6	72.0	177.5	177.6	52.5	181.5	181.6	22.8
173.6	173.7	43.8	177.6	177.7	52.9	181.6	181.7	28.1
173.7	173.8	96.9	177.7	177.8	56.1	181.7	181.8	49.7
173.8	173.9	80.0	177.8	177.9	60.0	181.8	181.9	40.9
173.9	174.0	78.1	177.9	178.0	55.1	181.9	182.0	16.9
174.0	174.1	73.9	178.0	178.1	61.4	182.0	182.1	32.0
182.1	182.2	45.8	183.8	183.9	74.3	185.5	185.6	31.0
182.2	182.3	54.7	183.9	184.0	89.7	185.6	185.7	31.3
182.3	182.4	39.4	184.0	184.1	37.9	185.7	185.8	57.5
182.4	182.5	25.3	184.1	184.2	29.2	185.8	185.9	47.5
182.5	182.6	15.6	184.2	184.3	33.7	185.9	186.0	35.6
182.6	182.7	31.5	184.3	184.4	23.4	186.0	186.1	43.8
182.7	182.8	42.9	184.4	184.5	28.0	186.1	186.2	51.5
182.8	182.9	49.9	184.5	184.6	41.7	186.2	186.3	42.7
182.9	183.0	45.2	184.6	184.7	40.9	186.3	186.4	27.7
183.0	183.1	75.3	184.7	184.8	36.1	186.4	186.5	29.2
183.1	183.2	80.2	184.8	184.9	76.4	186.5	186.6	39.2
183.2	183.3	49.5	184.9	185.0	50.1	186.6	186.7	15.4
183.3	183.4	52.6	185.0	185.1	44.2	186.7	186.8	19.4
183.4	183.5	28.7	185.1	185.2	33.7	186.8	186.9	27.7
183.5	183.6	44.4	185.2	185.3	30.1	186.9	187.0	40.3
183.6	183.7	46.6	185.3	185.4	40.6			
183.7	183.8	56.4	185.4	185.5	37.0			

Table A2
$\delta^{13}C_{org}$ and TOC Values Across the PETM Interval of the Bakchar Section

Hole	Sample	Depth (m)	$\delta^{13}C_{org}$ (‰)	TOC (%)
807	22	164	−26.4	0.37
807	23	166	−26.7	0.32
807	24	167.5	−27.6	0.34
807	30	168	−26.8	0.83
807	25	168.5	−27.2	0.21
807	31	169	−27.0	0.64
807	32	170.5	−26.6	0.14
807	33	172.5	−27.2	0.07
807	34	174.5	−25.4	0.11
807	35	176.5	−26.0	0.21
807	36	178.5	−25.9	0.13
807	37	180.2	−26.4	0.21
807	38	182	−25.5	0.09
807	26	183.5	−26.4	0.17
807	39	184	−26.3	0.25
807	40	186	−26.1	0.41
807	41	188	−26.1	0.40
807	42	190	−27.0	0.29

Table A3
Geochemical Parameters for Paleocene-Eocene Sediments From Hole 807 Through the Bakchar Deposit

Hole	Sample	Depth (m) m	Al (%) wt %	Fe (%) wt %	Fe EF	Mo EF	U EF	V EF	Ba_{bio} ppm	Zn EF	Cu EF	P EF	Ti EF
807	31	169	2.17	37.10	33.95	15.34	18.16	35.87	659.54	7.24	0.39	30.95	0.92
807	32	170.5	2.57	41.00	31.73	12.42	17.40	37.33	0.00	6.53	0.20	22.28	0.97
807	33	172.5	2.96	38.80	26.06	14.53	17.32	30.37	0.36	6.38	0.35	22.23	1.01
807	34	174.5	2.98	42.40	28.32	12.04	15.91	30.21	9.78	8.81	0.45	24.04	1.06
807	35	176.5	2.94	38.00	25.71	11.10	16.55	30.59	21.15	17.85	0.53	23.85	1.02
807	36	178.5	3.02	38.40	25.34	10.47	17.02	27.85	18.41	19.15	0.48	21.37	1.00
807	37	180.2	3.03	37.20	24.46	8.65	15.66	27.75	28.01	13.18	0.33	21.29	1.10
807	38	182	3.44	20.30	11.75	5.01	9.95	14.13	152.74	4.88	0.46	9.58	1.21
807	39	184	3.45	20.70	11.94	5.72	8.39	14.26	182.35	3.65	0.42	10.38	1.21
807	40	186	3.56	16.50	9.22	3.93	7.39	11.29	188.24	2.74	0.38	6.03	1.41
807	41	188	3.28	22.90	13.89	6.34	7.62	17.19	168.62	3.84	0.31	12.66	0.97
807	42	190	3.14	23.90	15.16	6.52	8.81	18.17	143.90	4.02	1.00	11.87	1.06

Acknowledgments
This study was supported by the Russian Foundation of Basic Research (grants 18–35-00022 and 16–45-700090) and by the Australian Research Council (grant DP140104544). Laboratory investigations were carried out at Tomsk Polytechnic University within the framework of a Tomsk Polytechnic University Competitiveness Enhancement Program grant. We thank N. Guseva, A. Khvashchevskaya, and I. Mazurova (Tomsk Polytechnic University) for assistance with geochemical analyses, and the Tomsk Oil and Gas Research and Design Institute for use of their mass spectrometer. We also thank the editor Y. Yokoyama, an anonymous reviewer, and Myriam Kars for their constructive reviews, which led to improvement of the manuscript. Supporting information is available from data repository Figshare (https://doi.org/10.6084/m9.figshare.5596858.v1).

References

Akhmetiev, M. A., & Zaporozhets, N. I. (2014). Paleogene events in Central Eurasia: Their role in the flora and vegetation cover evolution, migration of phytochore boundaries, and climate changes. *Stratigraphy and Geological Correlation*, *22*(3), 312–335. https://doi.org/10.1134/S0869593814030022

Alegret, L., Ortiz, S., Orue-Etxebarria, X., Bernaola, G., Baceta, J. I., Monechi, S.,. . . Pujalte, V. (2009). The Paleocene-Eocene Thermal Maximum: New data on microfossil turnover at the Zumaia section, Spain. *Palaios*, *24*(5–6), 318–328. https://doi.org/10.2110/palo.2008.p08-057r

Algeo, T. J., & Maynard, J. B. (2004). Trace-element behavior and redox facies in core shales of Upper Pennsylvanian Kansas-type cyclothems. *Chemical Geology*, *206*(3), 289–318. https://doi.org/10.1016/j.chemgeo.2003.12.009

Algeo, T. J., & Tribovillard, N. (2009). Environmental analysis of paleoceanographic systems based on molybdenum-uranium covariation. *Chemical Geology*, *268*(3), 211–225. https://doi.org/10.1016/j.chemgeo.2009.09.001

Baczynski, A. A., McInerney, F. A., Wing, S. L., Kraus, M. J., Bloch, J. I., & Secord, R. (2017). Constraining paleohydrologic change during the Paleocene-Eocene Thermal Maximum in the continental interior of North America. *Palaeogeography, Palaeoclimatology, Palaeoecology*, *465*, 237–246. https://doi.org/10.1016/j.palaeo.2016.10.030

Bains, S., Norris, R. D., Corfield, R. M., & Faul, K. L. (2000). Termination of global warmth at the Palaeocene/Eocene boundary through productivity feedback. *Nature*, *407*(6801), 171–174. https://doi.org/10.1038/35025035

Bakker, R. J., Dubessy, J., & Cathelineau, M. (1996). Improvements in clathrate modelling: I. The H_2O-CO_2 system with various salts. *Geochimica et Cosmochimica Acta*, *60*(10), 1657–1680. https://doi.org/10.1016/0016-7037(96)00032-4

Belous, N. C., Nikolaeva, I. V., Kazansky, Y. P., Berdnikov, A. P., Klyarovskiy, V. M., Kuznetsov, V. P., & Babin, A. A. (1964). *The Western-Siberian iron ore basin*. Novosibirsk: Siberian Branch of the Academy of Sciences of the USSR (in Russia).

Berner, R. A. (1969). Goethite stability and the origin of red beds. *Geochimica et Cosmochimica Acta*, *33*(2), 267–273. https://doi.org/10.1016/0016-7037(69)90143-4
Berner, R. A. (1981). A new geochemical classification of sedimentary environments. *Journal of Sedimentary Research*, *51*(2), 359–365.
Berner, R. A. (1984). Sedimentary pyrite formation: An update. *Geochimica et Cosmochimica Acta*, *48*(4), 605–615. https://doi.org/10.1016/0016-7037(84)90089-9
Boetius, A., Ravenschlag, K., Schubert, C. J., Rickert, D., Widdel, F., Gieseke, A.,. . . Pfannkuche, O. (2000). A marine microbial consortium apparently mediating anaerobic oxidation of methane. *Nature*, *407*(6804), 623–626. https://doi.org/10.1038/35036572
Boetius, A., & Wenzhöfer, F. (2013). Seafloor oxygen consumption fuelled by methane from cold seeps. *Nature Geoscience*, *6*(9), 725–734. https://doi.org/10.1038/ngeo1926
Bowen, G. J., Beerling, D. J., Koch, P. L., Zachos, J. C., & Quattlebaum, T. (2004). A humid climate state during the Palaeocene/Eocene thermal maximum. *Nature*, *432*(7016), 495–499. https://doi.org/10.1038/nature03115
Brumsack, H.-J. (2006). The trace metal content of recent organic carbon-rich sediments: Implications for Cretaceous black shale formation. *Palaeogeography, Palaeoclimatology, Palaeoecology*, *232*(2), 344–361. https://doi.org/10.1016/j.palaeo.2005.05.011
Calvert, S. E., & Pedersen, T. F. (1993). Geochemistry of recent oxic and anoxic marine sediments: Implications for the geological record. *Marine Geology*, *113*(1–2), 67–88. https://doi.org/10.1016/0025-3227(93)90150-T
Canfield, D. E., & Berner, R. A. (1987). Dissolution and pyritization of magnetite in anoxic marine sediments. *Geochimica et Cosmochimica Acta*, *51*(3), 645–659. https://doi.org/10.1016/0016-7037(87)90076-7
Carney, J. P., & Dick, T. A. (2000). The historical ecology of yellow perch (*Perca flavescens* [Mitchill]) and their parasites. *Journal of Biogeography*, *27*(6), 1337–1347. https://doi.org/10.1046/j.1365-2699.2000.00511.x
Carozza, D. A., Mysak, L. A., & Schmidt, G. A. (2011). Methane and environmental change during the Paleocene-Eocene thermal maximum (PETM): Modeling the PETM onset as a two-stage event. *Geophysical Research Letters*, *38*, L05702. https://doi.org/10.1029/2010GL046038
Chang, L., Vasiliev, I., van Baak, C., Krijgsman, W., Dekkers, M. J., Roberts, A. P.,. . . Winklhofer, M. (2014). Identification and environmental interpretation of diagenetic and biogenic greigite in sediments: A lesson from the Messinian Black Sea. *Geochemistry, Geophysics, Geosystems*, *15*, 3612–3627. https://doi.org/10.1002/2014GC005411
Cope, J. T., & Winguth, A. (2011). On the sensitivity of ocean circulation to Arctic freshwater input during the Paleocene/Eocene Thermal Maximum. *Palaeogeography, Palaeoclimatology, Palaeoecology*, *306*(1), 82–94. https://doi.org/10.1016/j.palaeo.2011.03.032
Crichton, K. A., Bouttes, N., Roche, D. M., Chappellaz, J., & Krinner, G. (2016). Permafrost carbon as a missing link to explain CO_2 changes during the last deglaciation. *Nature Geoscience*, *9*(9), 683–686. https://doi.org/10.1038/ngeo2793
Danise, S., Cavalazzi, B., Dominici, S., Westall, F., Monechi, S., & Guioli, S. (2012). Evidence of microbial activity from a shallow water whale fall (Voghera, northern Italy). *Palaeogeography, Palaeoclimatology, Palaeoecology*, *317*, 13–26. https://doi.org/10.1016/j.palaeo.2011.12.001
Dickens, G. R. (2011). Down the rabbit hole: Toward appropriate discussion of methane release from gas hydrate systems during the Paleocene-Eocene thermal maximum and other past hyperthermal events. *Climate of the Past*, *7*(3), 831–846. https://doi.org/10.5194/cp-7-831-2011
Dickens, G. R., Castillo, M. M., & Walker, J. C. G. (1997). A blast of gas in the latest Paleocene. *Geology*, *25*(3), 259–262.
Dickens, G. R., O'neil, J. R., Rea, D. K., & Owen, R. M. (1995). Dissociation of oceanic methane hydrate as a cause of the carbon isotope excursion at the end of the Paleocene. *Paleoceanography*, *10*(6), 965–971. https://doi.org/10.1029/95PA02087
Dickson, A. J., Cohen, A. S., Coe, A. L., Davies, M., Shcherbinina, E. A., & Gavrilov, Y. O. (2015). Evidence for weathering and volcanism during the PETM from Arctic Ocean and Peri-Tethys osmium isotope records. *Palaeogeography, Palaeoclimatology, Palaeoecology*, *438*, 300–307. https://doi.org/10.1016/j.palaeo.2015.08.019
Dickson, A. J., Rees-Owen, R. L., März, C., Coe, A. L., Cohen, A. S., Pancost, R. D.,. . . Shcherbinina, E. (2014). The spread of marine anoxia on the northern Tethys margin during the Paleocene-Eocene Thermal Maximum. *Paleoceanography*, *29*(6), 471–488. https://doi.org/10.1002/2014PA002629
Dill, H. G., Siegfanz, G., & Marchig, V. (1994). Mineralogy and chemistry of metalliferous muds forming the topstratum of a massive sulfide-metalliferous sediment sequence from East Pacific rise 18°S: Its origin and implications concerning the formation of ochrous sediments in cyprus-type deposits. *Marine Georesources and Geotechnology*, *12*(2), 159–180. https://doi.org/10.1080/10641199409388260
Dunkley Jones, T., Lunt, D. J., Schmidt, D. N., Ridgwell, A., Sluijs, A., Valdes, P. J., & Maslin, M. (2013). Climate model and proxy data constraints on ocean warming across the Paleocene-Eocene Thermal Maximum. *Earth-Science Reviews*, *125*, 123–145. https://doi.org/10.1016/j.earscirev.2013.07.004
Dymond, J., Suess, E., & Lyle, M. (1992). Barium in deep-sea sediment: A geochemical proxy for paleoproductivity. *Paleoceanography*, *7*(2), 163–181. https://doi.org/10.1029/92PA00181
Egger, M., Hagens, M., Sapart, C. J., Dijkstra, N., van Helmond, N. A. G. M., Mogollón, J. M.,. . . Slomp, C. P. (2017). Iron oxide reduction in methane-rich deep Baltic Sea sediments. *Geochimica et Cosmochimica Acta*, *207*, 256–276. https://doi.org/10.1016/j.gca.2017.03.019
Egger, M., Kraal, P., Jilbert, T., Sulu-Gambari, F., Sapart, C. J., Röckmann, T., & Slomp, C. P. (2016). Anaerobic oxidation of methane alters sediment records of sulfur, iron and phosphorus in the Black Sea. *Biogeosciences*, *13*(18), 5333–5355. https://doi.org/10.5194/bg-13-5333-2016
El-Habaak, G., Askalany, M., Faraghaly, M., & Abdel-Hakeem, M. (2016). The economic potential of El-Gedida glauconite deposits, El-Bahariya Oasis, Western Desert, Egypt. *Journal of African Earth Sciences*, *120*, 186–197. https://doi.org/10.1016/j.jafrearsci.2016.05.007
Etiope, G., & Klusman, R. W. (2002). Geologic emissions of methane to the atmosphere. *Chemosphere*, *49*(8), 777–789. https://doi.org/10.1016/S0045-6535(02)00380-6
Fontorbe, G., Frings, P. J., de la Rocha, C. L., Hendry, K. R., & Conley, D. J. (2016). A silicon depleted North Atlantic since the Palaeogene: Evidence from sponge and radiolarian silicon isotopes. *Earth and Planetary Science Letters*, *453*, 67–77. https://doi.org/10.1016/j.epsl.2016.08.006
Frezzotti, M. L., Tecce, F., & Casagli, A. (2012). Raman spectroscopy for fluid inclusion analysis. *Journal of Geochemical Exploration*, *112*, 1–20. https://doi.org/10.1016/j.gexplo.2011.09.009
Frieling, J., Iakovleva, A. I., Reichart, G.-J., Aleksandrova, G. N., Gnibidenko, Z. N., Schouten, S., & Sluijs, A. (2014). Paleocene-Eocene warming and biotic response in the epicontinental West Siberian Sea. *Geology*, *42*(9), 767–770. https://doi.org/10.1130/G35724.1
Froelich, P. N., Klinkhammer, G. P., Bender, M. L., Luedtke, N. A., Heath, G. R., Cullen, D.,. . . Maynard, V. (1979). Early oxidation of organic matter in pelagic sediments of the eastern equatorial Atlantic: Suboxic diagenesis. *Geochimica et Cosmochimica Acta*, *43*(7), 1075–1090. https://doi.org/10.1016/0016-7037(79)90095-4
Gibbs, S. J., Bown, P. R., Murphy, B. H., Sluijs, A., Edgar, K. M., Pälike, H.,. . . Zachos, J. C. (2012). Scaled biotic disruption during early Eocene global warming events. *Biogeosciences*, *9*, 4679–4688. https://doi.org/10.5194/bg-9-4679-2012
Gnibidenko, Z. N., Lebedeva, N. K., & Levicheva, A. V. (2015). Magnetostratigraphy of the Campanian-Maastrichtian Bakchar Basin (southeastern West Siberia). *Russian Geology and Geophysics*, *56*(11), 1652–1661. https://doi.org/10.1016/j.rgg.2015.10.011

Griffith, E. M., Fantle, M. S., Eisenhauer, A., Paytan, A., & Bullen, T. D. (2015). Effects of ocean acidification on the marine calcium isotope record at the Paleocene-Eocene Thermal Maximum. *Earth and Planetary Science Letters*, *419*, 81–92. https://doi.org/10.1016/j.epsl.2015.03.010

Higgins, J. A., & Schrag, D. P. (2006). Beyond methane: Towards a theory for the Paleocene-Eocene Thermal Maximum. *Earth and Planetary Science Letters*, *245*(3), 523–537. https://doi.org/10.1016/j.epsl.2006.03.009

Horng, C.-S., & Chen, K.-H. (2006). Complicated magnetic mineral assemblages in marine sediments offshore of southwestern Taiwan: Possible influence of methane flux on the early diagenetic process. *Terrestrial, Atmospheric and Oceanic Sciences*, *17*(4), 1009–1026.

Horng, C.-S., & Huh, C.-A. (2011). Magnetic properties as tracers for source-to-sink dispersal of sediments: A case study in the Taiwan Strait. *Earth and Planetary Science Letters*, *309*(1), 141–152. https://doi.org/10.1016/j.epsl.2011.07.002

Horng, C.-S., Huh, C. A., Chen, K. H., Lin, C. H., Shea, K. S., & Hsiung, K. H. (2012). Pyrrhotite as a tracer for denudation of the Taiwan orogen. *Geochemistry, Geophysics, Geosystems*, *13*, Q08Z47. https://doi.org/10.1029/2012GC004195

Horng, C.-S., & Roberts, A. P. (2006). Authigenic or detrital origin of pyrrhotite in sediments? Resolving a paleomagnetic conundrum. *Earth and Planetary Science Letters*, *241*(3), 750–762. https://doi.org/10.1016/j.epsl.2005.11.008

Horng, C.-S., Torii, M., Shea, K.-S., & Kao, S.-J. (1998). Inconsistent magnetic polarities between greigite- and pyrrhotite/magnetite-bearing marine sediments from the Tsailiao-chi section, southwestern Taiwan. *Earth and Planetary Science Letters*, *164*(3), 467–481. https://doi.org/10.1016/S0012-821X(98)00239-8

Housen, B. A., & Musgrave, R. J. (1996). Rock-magnetic signature of gas hydrates in accretionary prism sediments. *Earth and Planetary Science Letters*, *139*(3–4), 509–519. https://doi.org/10.1016/0012-821X(95)00245-8

Iakovleva, A. I. (2011). Palynological reconstruction of the Eocene marine palaeoenvironments in south of western Siberia. *Acta Palaeobotanica*, *51*(2), 229–248.

Jaramillo, C., Rueda, M. J., & Mora, G. (2006). Cenozoic plant diversity in the neotropics. *Science*, *311*(5769), 1893–1896.

Jiang, S., Park, S., Yoon, Y., Lee, J.-H., Wu, W.-M., Phuoc Dan, N.,. . . Hur, H.-G. (2013). Methanogenesis facilitated by geobiochemical iron cycle in a novel syntrophic methanogenic microbial community. *Environmental Science and Technology*, *47*(17), 10078–10084. https://doi.org/10.1021/es402412c

Jørgensen, B. B., Böttcher, M. E., Lüschen, H., Neretin, L. N., & Volkov, I. I. (2004). Anaerobic methane oxidation and a deep H_2S sink generate isotopically heavy sulfides in Black Sea sediments. *Geochimica et Cosmochimica Acta*, *68*(9), 2095–2118. https://doi.org/10.1016/j.gca.2003.07.017

Jørgensen, B. B., & Kasten, S. (2006). Sulfur cycling and methane oxidation. In *Marine geochemistry* (pp. 271–309). Berlin, Heidelberg: Springer.

Kars, M., & Kodama, K. (2015a). Authigenesis of magnetic minerals in gas hydrate-bearing sediments in the Nankai Trough, offshore Japan. *Geochemistry, Geophysics, Geosystems*, *16*, 947–961. https://doi.org/10.1002/2014GC005614

Kars, M., & Kodama, K. (2015b). Rock magnetic characterization of ferrimagnetic iron sulfides in gas hydrate-bearing marine sediments at Site C0008, Nankai Trough, Pacific Ocean, off-coast Japan. *Earth, Planets and Space*, *67*, 1–12. https://doi.org/10.1186/s40623-015-0287-y

Kasten, S., Freudenthal, T., Gingele, F. X., & Schulz, H. D. (1998). Simultaneous formation of iron-rich layers at different redox boundaries in sediments of the Amazon deep-sea fan. *Geochimica et Cosmochimica Acta*, *62*(13), 2253–2264. https://doi.org/10.1016/S0016-7037(98)00093-3

Kato, S., Hashimoto, K., & Watanabe, K. (2012). Methanogenesis facilitated by electric syntrophy via (semi)conductive iron-oxide minerals. *Environmental Microbiology*, *14*(7), 1646–1654. https://doi.org/10.1111/j.1462-2920.2011.02611.x

Kennett, J. P., & Stott, L. D. (1991). Abrupt deep-sea warming, paleoceanographic changes and benthic extinctions at the end of the Paleocene. *Nature*, *353*, 225–229.

Koch, P. L., Zachos, J. C., & Gingerich, P. D. (1992). Correlation between isotope records in marine and continental carbon reservoirs near the Paleocene/Eocene boundary. *Nature*, *358*, 319–322.

Kopp, R. E., Schumann, D., Raub, T. D., Powars, D. S., Godfrey, L. V., Swanson-Hysell, N. L.,. . . Vali, H. (2009). An Appalachian Amazon? Magnetofossil evidence for the development of a tropical river-like system in the mid-Atlantic United States during the Paleocene-Eocene thermal maximum. *Paleoceanography*, *24*(4), 1–17. https://doi.org/10.1029/2009PA001783

Kvenvolden, K. A. (1993). Gas hydrates—Geological perspective and global change. *Reviews of Geophysics*, *31*, 173–187.

Kvenvolden, K. A., & Rogers, B. W. (2005). Gaia's breath—Global methane exhalations. *Marine and Petroleum Geology*, *22*(4), 579–590. https://doi.org/10.1016/j.marpetgeo.2004.08.004

Labrenz, M., Druschel, G. K., Thomsen-Ebert, T., Gilbert, B., Welch, S. A., Kemner, K. M.,. . . Banfield, J. F. (2000). Formation of sphalerite (ZnS) deposits in natural biofilms of sulfate-reducing bacteria. *Science*, *290*(5497), 1744–1747.

Larrasoaña, J. C., Roberts, A. P., Musgrave, R. J., Gràcia, E., Piñero, E., Vega, M., & Martínez-Ruiz, F. (2007). Diagenetic formation of greigite and pyrrhotite in gas hydrate marine sedimentary systems. *Earth and Planetary Science Letters*, *261*(3), 350–366. https://doi.org/10.1016/j.epsl.2007.06.032

Lebedel, V., Lezin, C., Andreu, B., Wallez, M.-J., Ettachfini, E. M., & Riquier, L. (2013). Geochemical and palaeoecological record of the Cenomanian-Turonian Anoxic Event in the carbonate platform of the Preafrican Trough, Morocco. *Palaeogeography, Palaeoclimatology, Palaeoecology*, *369*, 79–98. https://doi.org/10.1016/j.palaeo.2012.10.005

Lebedeva, N. K., Kuzmina, O. B., Sobolev, E. S., & Khazina, I. V. (2017). Stratigraphy of Upper Cretaceous and Cenozoic deposits of the Bakchar iron ore deposit (southwestern Siberia): New data. *Stratigraphy and Geological Correlation*, *25*(1), 76–98. https://doi.org/10.1134/S0869593817010038

Lin, Q., Wang, J., Algeo, T. J., Sun, F., & Lin, R. (2016). Enhanced framboidal pyrite formation related to anaerobic oxidation of methane in the sulfate-methane transition zone of the northern South China Sea. *Marine Geology*, *379*, 100–108. https://doi.org/10.1016/j.margeo.2016.05.016

Liu, J., Zhu, R., Roberts, A. P., Li, S., & Chang, J. (2004). High-resolution analysis of early diagenetic effects on magnetic minerals in post-middle-Holocene continental shelf sediments from the Korea Strait. *Journal of Geophysical Research*, *109*, B03103. https://doi.org/10.1029/2003JB002813

Lourens, L. J., Sluijs, A., Kroon, D., Zachos, J. C., Thomas, E., Röhl, U.,. . . Raffi, I. (2005). Astronomical pacing of late Palaeocene to early Eocene global warming events. *Nature*, *435*(7045), 1083–1087. https://doi.org/10.1038/nature03814

Lovley, D. R., & Phillips, E. J. (1986). Organic matter mineralization with reduction of ferric iron in anaerobic sediments. *Applied and Environmental Microbiology*, *51*, 683–689.

Lu, W., Chou, I. M., & Burruss, R. C. (2008). Determination of methane concentrations in water in equilibrium with sI methane hydrate in the absence of a vapor phase by in situ Raman spectroscopy. *Geochimica et Cosmochimica Acta*, *72*(2), 412–422. https://doi.org/10.1016/j.gca.2007.11.006

Lunt, D. J., Valdes, P. J., Jones, T. D., Ridgwell, A., Haywood, A. M., Schmidt, D. N.,. . . Maslin, M. (2010). CO_2-driven ocean circulation changes as an amplifier of Paleocene-Eocene thermal maximum hydrate destabilization. *Geology*, *38*(10), 875–878. https://doi.org/10.1130/G31184.1

Manners, H. R., Grimes, S. T., Sutton, P. A., Domingo, L., Leng, M. J., Twitchett, R. J.. . ., Lopez-Martinez, N. (2013). Magnitude and profile of organic carbon isotope records from the Paleocene-Eocene Thermal Maximum: Evidence from northern Spain. *Earth and Planetary Science Letters*, *376*, 220–230. https://doi.org/10.1016/j.epsl.2013.06.016

McInerney, F. A., & Wing, S. L. (2011). The Paleocene-Eocene Thermal Maximum: A perturbation of carbon cycle, climate, and biosphere with implications for the future. *Annual Review of Earth and Planetary Sciences*, *39*(1), 489–516. https://doi.org/10.1146/annurev-earth-040610-133431

Meissner, K. J., Bralower, T. J., Alexander, K., Jones, T. D., Sijp, W., & Ward, M. (2014). The Paleocene-Eocene Thermal Maximum: How much carbon is enough? *Paleoceanography*, *29*(10), 946–963. https://doi.org/10.1002/2014PA002650

Monnin, E. (2001). Atmospheric CO_2 concentrations over the Last Glacial Termination. *Science*, *291*(5501), 112–114. https://doi.org/10.1126/science.291.5501.112

Morales, C., Kujau, A., Heimhofer, U., Mutterlose, J., Spangenberg, J. E., Adatte, T.,. . . Föllmi, K. B. (2015). Palaeoclimate and palaeoenvironmental changes through the onset of the Valanginian carbon-isotope excursion: Evidence from the Polish Basin. *Palaeogeography, Palaeoclimatology, Palaeoecology*, *426*, 183–198. https://doi.org/10.1016/j.palaeo.2015.03.013

Mücke, A. (2006). Chamosite, siderite and the environmental conditions of their formation in chamosite-type Phanerozoic ooidal ironstones. *Ore Geology Reviews*, *28*(2), 235–249. https://doi.org/10.1016/j.oregeorev.2005.03.004

Munch, J. C., & Ottow, J. C. G. (1983). Reductive transformation mechanism of ferric oxides in hydromorphic soils. *Environmental Biogeochemistry Ecological Bulletins*, *35*, 383–394.

Murphy, A. E., Sageman, B. B., Hollander, D. J., Lyons, T. W., & Brett, C. E. (2000). Black shale deposition and faunal overturn in the Devonian Appalachian Basin: Clastic starvation, seasonal water-column mixing, and efficient biolimiting nutrient recycling. *Paleoceanography*, *15*(3), 280–291. https://doi.org/10.1029/1999PA000445

Neretin, L. N., Böttcher, M. E., Jørgensen, B. B., Volkov, I. I., Lüschen, H., & Hilgenfeldt, K. (2004). Pyritization processes and greigite formation in the advancing sulfidization front in the upper Pleistocene sediments of the Black Sea. *Geochimica et Cosmochimica Acta*, *68*(9), 2081–2093. https://doi.org/10.1016/S0016-7037(03)00450-2

Nunes, F., & Norris, R. D. (2006). Abrupt reversal in ocean overturning during the Palaeocene/Eocene warm period. *Nature*, *439*(7072), 60–63. https://doi.org/10.1038/nature04386

Núñez-Useche, F., Canet, C., Barragán, R., & Alfonso, P. (2016). Bioevents and redox conditions around the Cenomanian-Turonian anoxic event in Central Mexico. *Palaeogeography, Palaeoclimatology, Palaeoecology*, *449*, 205–226. https://doi.org/10.1016/j.palaeo.2016.01.035

Pälike, C., Delaney, M. L., & Zachos, J. C. (2014). Deep-sea redox across the Paleocene-Eocene thermal maximum. *Geochemistry, Geophysics, Geosystems*, *15*, 1038–1053. https://doi.org/10.1002/2013GC005074

Panchuk, K., Ridgwell, A., & Kump, L. R. (2008). Sedimentary response to Paleocene-Eocene thermal maximum carbon release: A model-data comparison. *Geology*, *36*(4), 315–318. https://doi.org/10.1130/G24474A.1

Penman, D. E. (2016). Silicate weathering and North Atlantic silica burial during the Paleocene-Eocene Thermal Maximum. *Geology*, *44*(9), 731–734. https://doi.org/10.1130/G37704.1

Penman, D. E., Hönisch, B., Zeebe, R. E., Thomas, E., & Zachos, J. C. (2014). Rapid and sustained surface ocean acidification during the Paleocene-Eocene Thermal Maximum. *Paleoceanography*, *29*(5), 357–369. https://doi.org/10.1002/2014PA002621

Penman, D. E., Turner, K. S., Sexton, P., Norris, R., Dickson, A. J., Boulila, S.,. . . Röhl, U. (2015). A carbonate compensation depth overshoot in the aftermath of the Paleocene-Eocene Thermal Maximum. *Nature Geoscience*, *9*(8), 575–580. https://doi.org/10.1038/ngeo2757

Pironon, J., Sawatzki, J., & Dubessy, J. (1991). Letter: NIR FT-Raman microspectroscopy of fluid inclusions: Comparisons with VIS Raman and FT-IR microspectroscopies. *Geochimica et Cosmochimica Acta*, *55*(12), 3885–3891. https://doi.org/10.1016/0016-7037(91)90083-H

Podobina, V. (2015). Regional stratigraphy and its dependency on tectonic movements (case study: Upper Cretaceous and Paleogene stages in Western Siberia). *IOP Conference Series: Earth and Environmental Science*, *24*(1), 12012. https://doi.org/10.1088/1755-1315/24/1/012012

Podobina, V. M. (1998). Substantiation of the Paleocene-Eocene boundary in western Siberia by foraminifers. *Stratigraphy and Geological Correlation*, *6*(2), 142–149.

Podobina, V. M. (2003). Paleocene biota of the West Siberian Plain. In *Special paper 369: Causes and consequences of globally warm climates in the early Paleogene* (Vol. 369, pp. 181–204). Boulder, CO: Geological Society of America.

Pósfai, M., Cziner, K., Márton, E., Márton, P., Buseck, P. R., Frankel, R. R. B., & Bazylinski, D. A. (2001). Crystal-size distributions and possible biogenic origin of Fe sulfides. *European Journal of Mineralogy*, *13*(4), 691–703. https://doi.org/10.1127/0935-1221/2001/0013-0691

Rachold, V., & Brumsack, H.-J. (2001). Inorganic geochemistry of Albian sediments from the Lower Saxony Basin NW Germany: Palaeoenvironmental constraints and orbital cycles. *Palaeogeography, Palaeoclimatology, Palaeoecology*, *174*(1), 121–143. https://doi.org/10.1016/S0031-0182(01)00290-5

Reitz, A., Pfeifer, K., de Lange, G., & Klump, J. (2004). Biogenic barium and the detrital Ba/Al ratio: A comparison of their direct and indirect determination. *Marine Geology*, *204*(3), 289–300. https://doi.org/10.1016/S0025-3227(04)00004-0

Riedinger, N., Pfeifer, K., Kasten, S., Garming, J. F. L., Vogt, C., & Hensen, C. (2005). Diagenetic alteration of magnetic signals by anaerobic oxidation of methane related to a change in sedimentation rate. *Geochimica et Cosmochimica Acta*, *69*(16), 4117–4126. https://doi.org/10.1016/j.gca.2005.02.004

Riquier, L., Tribovillard, N., Averbuch, O., Devleeschouwer, X., & Riboulleau, A. (2006). The Late Frasnian Kellwasser horizons of the Harz Mountains (Germany): Two oxygen-deficient periods resulting from different mechanisms. *Chemical Geology*, *233*(1), 137–155. https://doi.org/10.1016/j.chemgeo.2006.02.021

Roberts, A. P. (2015). Magnetic mineral diagenesis. *Earth-Science Reviews*, *151*, 1–47. https://doi.org/10.1016/j.earscirev.2015.09.010

Roberts, A. P., Chang, L., Rowan, C. J., Horng, C.-S., & Florindo, F. (2011). Magnetic properties of sedimentary greigite (Fe_3S_4): An update. *Reviews of Geophysics*, *49*, RG1002. https://doi.org/10.1029/2010RG000336

Roberts, A. P., Florindo, F., Larrasoaña, J. C., O'regan, M. A., & Zhao, X. (2010). Complex polarity pattern at the former Plio-Pleistocene global stratotype section at Vrica (Italy): Remagnetization by magnetic iron sulphides. *Earth and Planetary Science Letters*, *292*(1), 98–111. https://doi.org/10.1016/j.epsl.2010.01.025

Roberts, A. P., & Turner, G. M. (1993). Diagenetic formation of ferrimagnetic iron sulphide minerals in rapidly deposited marine sediments, South Island, New Zealand. *Earth and Planetary Science Letters*, *115*(1–4), 257–273. https://doi.org/10.1016/0012-821X(93)90226-Y

Roberts, A. P., & Weaver, R. (2005). Multiple mechanisms of remagnetization involving sedimentary greigite (Fe_3S_4). *Earth and Planetary Science Letters*, *231*(3), 263–277. https://doi.org/10.1016/j.epsl.2004.11.024

Röhl, U., Westerhold, T., Bralower, T. J., & Zachos, J. C. (2007). On the duration of the Paleocene-Eocene thermal maximum (PETM). *Geochemistry, Geophysics, Geosystems*, *8*, Q12002. https://doi.org/10.1029/2007GC001784

Rudmin, M. A., & Mazurov, A. K. (2016). Oolitic ores in the Bakchar iron-ore cluster (Tomsk Oblast). *Doklady Earth Sciences*, *471*(2), 1238–1241. https://doi.org/10.1134/S1028334X16120126

Schmitz, B., Asaro, F., Molina, E., Monechi, S., von Salis, K., & Speijer, R. P. (1997). High-resolution iridium, $\delta^{13}C$, $\delta^{18}O$, foraminifera and nannofossil profiles across the latest Paleocene benthic extinction event at Zumaya, Spain. *Palaeogeography, Palaeoclimatology, Palaeoecology*, *133*(1–2), 49–68. https://doi.org/10.1016/S0031-0182(97)00024-2

Schubert, F., Diamond, L. W., & Tóth, T. M. (2007). Fluid-inclusion evidence of petroleum migration through a buried metamorphic dome in the Pannonian Basin, Hungary. *Chemical Geology*, *244*(3–4), 357–381. https://doi.org/10.1016/j.chemgeo.2007.05.019

Seewald, J. S., Seyfried, W. E., & Thornton, E. C. (1990). Organic-rich sediment alteration: An experimental and theoretical study at elevated temperatures and pressures. *Applied Geochemistry*, *5*(1–2), 193–209. https://doi.org/10.1016/0883-2927(90)90048-A

Shakhova, N., Semiletov, I., Gustafsson, O., Sergienko, V., Lobkovsky, L., Dudarev, O.,. . . Chernykh, D. (2017). Current rates and mechanisms of subsea permafrost degradation in the East Siberian Arctic Shelf. *Nature Communications*, *8*, 1–13. https://doi.org/10.1038/ncomms15872

Shcherbinina, E., Gavrilov, Y., Iakovleva, A., Pokrovsky, B., Golovanova, O., & Aleksandrova, G. (2016). Environmental dynamics during the Paleocene-Eocene thermal maximum (PETM) in the northeastern Peri-Tethys revealed by high-resolution micropalaeontological and geochemical studies of a Caucasian key section. *Palaeogeography, Palaeoclimatology, Palaeoecology*, *456*, 60–81. https://doi.org/10.1016/j.palaeo.2016.05.006

Shi, M., Wu, H., Roberts, A. P., Zhang, S., Zhao, X., Li, H.,. . . Wang, H. (2017). Tectonic, climatic, and diagenetic control of magnetic properties of sediments from Kumano Basin, Nankai margin, southwestern Japan. *Marine Geology*, *391*, 1–12. https://doi.org/10.1016/j.margeo.2017.07.006

Sivan, O., Shusta, S. S., & Valentine, D. L. (2016). Methanogens rapidly transition from methane production to iron reduction. *Geobiology*, *14*(2), 190–203. https://doi.org/10.1111/gbi.12172

Smith, A. G., Smith, D. G., & Funnell, B. M. (1994). *Atlas of Mesozoic and Cenozoic coastlines*. Cambridge, UK: Cambridge University Press.

Stassen, P., Thomas, E., & Speijer, R. P. (2015). Paleocene-Eocene Thermal Maximum environmental change in the New Jersey Coastal Plain: Benthic foraminiferal biotic events. *Marine Micropaleontology*, *115*, 1–23. https://doi.org/10.1016/j.marmicro.2014.12.001

Taylor, S. R., & McLennan, S. M. (1985). *The continental crust: Its composition and evolution. An examination of the geochemical record preserved in sedimentary rocks*. Oxford, UK: Blackwell.

Tesi, T., Muschitiello, F., Smittenberg, R. H., Jakobsson, M., Vonk, J. E., Hill, P.,. . . Gustafsson, Ö. (2016). Massive remobilization of permafrost carbon during post-glacial warming. *Nature Communications*, *7*, 13653. https://doi.org/10.1038/ncomms13653

Thomas, D. J., Zachos, J. C., Bralower, T. J., Thomas, E., & Bohaty, S. (2002). Warming the fuel for the fire: Evidence for the thermal dissociation of methane hydrate during the Paleocene-Eocene thermal maximum. *Geology*, *30*(12), 1067–1070. https://doi.org/10.1130/0091-7613(2002)030<1067:WTFFTF>2.0.CO;2

Thomas, E., & Shackleton, N. J. (1996). The Paleocene-Eocene benthic foraminiferal extinction and stable isotope anomalies. *Geological Society Special Publications*, *101*(1), 401–441. https://doi.org/10.1144/GSL.SP.1996.101.01.20

Tribovillard, N., Algeo, T. J., Baudin, F., & Riboulleau, A. (2012). Analysis of marine environmental conditions based on molybdenum-uranium covariation—Applications to Mesozoic paleoceanography. *Chemical Geology*, *324*, 46–58. https://doi.org/10.1016/j.chemgeo.2011.09.009

Tribovillard, N., Algeo, T. J., Lyons, T., & Riboulleau, A. (2006). Trace metals as paleoredox and paleoproductivity proxies: An update. *Chemical Geology*, *232*(1), 12–32. https://doi.org/10.1016/j.chemgeo.2006.02.012

van Dongen, B. E., Roberts, A. P., Schouten, S., Jiang, W.-T., Florindo, F., & Pancost, R. D. (2007). Formation of iron sulfide nodules during anaerobic oxidation of methane. *Geochimica et Cosmochimica Acta*, *71*(21), 5155–5167. https://doi.org/10.1016/j.gca.2007.08.019

Vasiliev, I., Franke, C., Meeldijk, J. D., Dekkers, M. J., Langereis, C. G., & Krijgsman, W. (2008). Putative greigite magnetofossils from the Pliocene Epoch. *Nature Geoscience*, *1*(11), 782–786. https://doi.org/10.1038/ngeo335

Vibe, Y., Bunge, H.-P., & Clark, S. R. (2017). Anomalous subsidence history of the West Siberian Basin as an indicator for episodes of mantle induced dynamic topography. *Gondwana Research*, *53*, 99–109. https://doi.org/10.1016/j.gr.2017.03.011.

Weaver, R., Roberts, A. P., & Barker, A. J. (2002). A late diagenetic (syn-folding) magnetization carried by pyrrhotite: Implications for paleomagnetic studies from magnetic iron sulphide-bearing sediments. *Earth and Planetary Science Letters*, *200*(3), 371–386. https://doi.org/10.1016/S0012-821X(02)00652-0

Wei, H., Algeo, T. J., Yu, H., Wang, J., Guo, C., & Shi, G. (2015). Episodic euxinia in the Changhsingian (late Permian) of South China: Evidence from framboidal pyrite and geochemical data. *Sedimentary Geology*, *319*, 78–97. https://doi.org/10.1016/j.sedgeo.2014.11.008

Westbrook, G. K., Thatcher, K. E., Rohling, E. J., Piotrowski, A. M., Pälike, H., Osborne, A. H.,. . . Aquilina, A. (2009). Escape of methane gas from the seabed along the West Spitsbergen continental margin. *Geophysical Research Letters*, *36*, L15608. https://doi.org/10.1029/2009GL039191

Wing, S. L., Harrington, G. J., Smith, F. A., Bloch, J. I., Boyer, D. M., & Freeman, K. H. (2005). Transient floral change and rapid global warming at the Paleocene-Eocene boundary. *Science*, *310*(5750), 993–996.

Yamamoto, A., Yamanaka, Y., & Tajika, E. (2009). Modeling of methane bubbles released from large sea-floor area: Condition required for methane emission to the atmosphere. *Earth and Planetary Science Letters*, *284*(3–4), 590–598. https://doi.org/10.1016/j.epsl.2009.05.026

Zachos, J. C., Dickens, G. R., & Zeebe, R. E. (2008). An early Cenozoic perspective on greenhouse warming and carbon-cycle dynamics. *Nature*, *451*(7176), 279–283. https://doi.org/10.1038/nature06588

Zachos, J. C., Wara, M. W., Bohaty, S., Delaney, M. L., Petrizzo, M. R., Brill, A.,. . . Premoli-Silva, I. (2003). A transient rise in tropical sea surface temperature during the Paleocene-Eocene Thermal Maximum. *Science*, *302*(5650), 1551–1554.

Zeebe, R. E. (2013). What caused the long duration of the Paleocene-Eocene Thermal Maximum? *Paleoceanography*, *28*(3), 440–452. https://doi.org/10.1002/palo.20039

Zeebe, R. E., Ridgwell, A., & Zachos, J. C. (2016). Anthropogenic carbon release rate unprecedented during the past 66 million years. *Nature Geoscience*, *9*(4), 325–329. https://doi.org/10.1038/ngeo2681

Zeebe, R. E., & Zachos, J. C. (2007). Reversed deep-sea carbonate ion basin gradient during Paleocene-Eocene thermal maximum. *Paleoceanography*, *22*, PA3201. https://doi.org/10.1029/2006PA001395

Zhang, Q., Wendler, I., Xu, X., Willems, H., & Ding, L. (2017). Structure and magnitude of the carbon isotope excursion during the Paleocene-Eocene thermal maximum. *Gondwana Research*, *46*, 114–123. https://doi.org/10.1016/j.gr.2017.02.016